CH Mode Mixing Determines the Bandshape of Carboxylate Symmetric Stretch in Apo, Ca^{2+}, and Mg^{2+} – EDTA

Sunayana Mitra,[†] Keith Werling,[‡] Eric J. Berquist,[¶] Daniel S. Lambrecht,[†,§] and Sean Garrett-Roe[*,†]

†*Department of Chemistry, University of Pittsburgh, Pittsburgh, PA 15260*

‡*School of Medicine, University of Pittsburgh, Pittsburgh, PA 15260*

¶*Q-Chem Incorporated, 6601 Owens Drive, Suite 105, Pleasanton, CA 94588*

§*Department of Chemistry and Physics, Florida Gulf Coast University, Fort Myers, FL 33965*

E-mail: sgr@pitt.edu

Phone: +1 412 624 1283. Fax: +1 412 624 8611

Abstract

The infrared spectra of EDTA complexed with Ca^{2+} and Mg^{2+} contain, to date, unidentified vibrational bands.This study assigns the peaks in the linear and two-dimensional infrared spectra of EDTA, with and without either Ca^{2+} or Mg^{2+} ions. Two-dimensional infrared spectroscopy and DFT calculations reveal that in both the presence and absence of ions, the carboxylate symmetric stretch and the terminal CH bending vibrations mix. We introduce a method to calculate participation coefficients that quantify the contribution of the carboxylate symmetric stretch, CH wag, CH twist, and CH scissor in the 1400–1550 cm^{-1} region. With the help of participation coefficients, we assign the 1400–1430 cm^{-1} region to the carboxylate symmetric stretch which can mix with CH modes. We assign the 1000–1380 cm^{-1} region to CH twist modes, the 1380–1430 cm^{-1} region to wag modes, and the 1420–1650 cm^{-1} region to scissor modes. The difference in binding geometry between the carboxylate-Ca^{2+} and carboxylate-Mg^{2+} complex manifests as new diagonal and cross-peaks between the mixed modes in the two complexes. The small Mg^{2+} ion binds EDTA tighter than the Ca^{2+} ion, which causes a redshift of the COOs modes of the sagittal carboxylates. Energy decomposition analysis further characterizes the importance of electrostatics and deformation energy in the bound complexes.

Keywords EDTA, ultrafast vibrational spectroscopy, 2D-IR, mixed-mode, vibrational coupling, Ca^{2+}, Mg^{2+}, cross-peaks, normal mode, DFT, M05-2X, def2-TZVP, ωB97X-D, participation coefficient, EDA, ALMO-EDA, SAPT0.

1 Introduction

Ethylenediaminetetraacetic acid (EDTA) can model divalent ion–carboxylate interactions in proteins.[1–3] In the broad class of EF-hand proteins, for example, divalent ion-binding induces structural changes[4] and begins a cascade of protein folding,[5] cell signaling,[5] ion transport,[5] ion recognition,[5] and enzyme activation events.[6–10] Binding selectivity and affinity of Ca^{2+} over Mg^{2+} is critical for the biological function of these proteins.

Though EDTA mimics the EF-hand binding pocket, spectroscopic studies fail to unambiguously correlate metal binding geometries with the positions and intensities of the carboxylate vibrational bands.[11–17] The additional information content of two dimensional infrared (2D-IR) spectroscopy promises to allow more direct relationships between observed spectral features and ion–binding geometries. Additionally, it can provide insight into the femtosecond and picosecond dynamics in the binding pocket.[18–21]

In the absence of divalent ions, EDTA has an extended, flexible structure in solution. Upon metal binding, EDTA assumes an approximately C_2 symmetry (Figure 1). The pairs of carboxylates lie in two planes. In the 'sagittal' plane (along the violet line), the two carboxylates are oriented parallel to each other, while the other two carboxylates are oriented antiparallel to one another and lie rotated slightly out of the 'equatorial' plane. The binding geometries of calcium- and magnesium-bound EDTA, $[Ca{:}EDTA]^{2-}$ and $[Mg{:}EDTA]^{2-}$, respectively, differ subtly. The smaller Mg^{2+} ion lies deeper in the binding pocket and the terminal oxygens approach the Mg^{2+} more closely. These differences cause changes in the NCCO dihedral angles along each of the carboxylates. These subtle rearrangements are similar to the structural differences between Ca^{2+}- and Mg^{2+}-bound EF-hands. If spectroscopic observables could be related to these differences in geometry, they might prove a powerful tool for determining the mechanism of ion selectivity in EF-hand proteins.

2D-IR spectroscopy is highly sensitive to local picosecond fluctuations, environmental dynamics, and molecular structure.[21,22] Techniques like X-ray crystallography[23] and EPR[24]

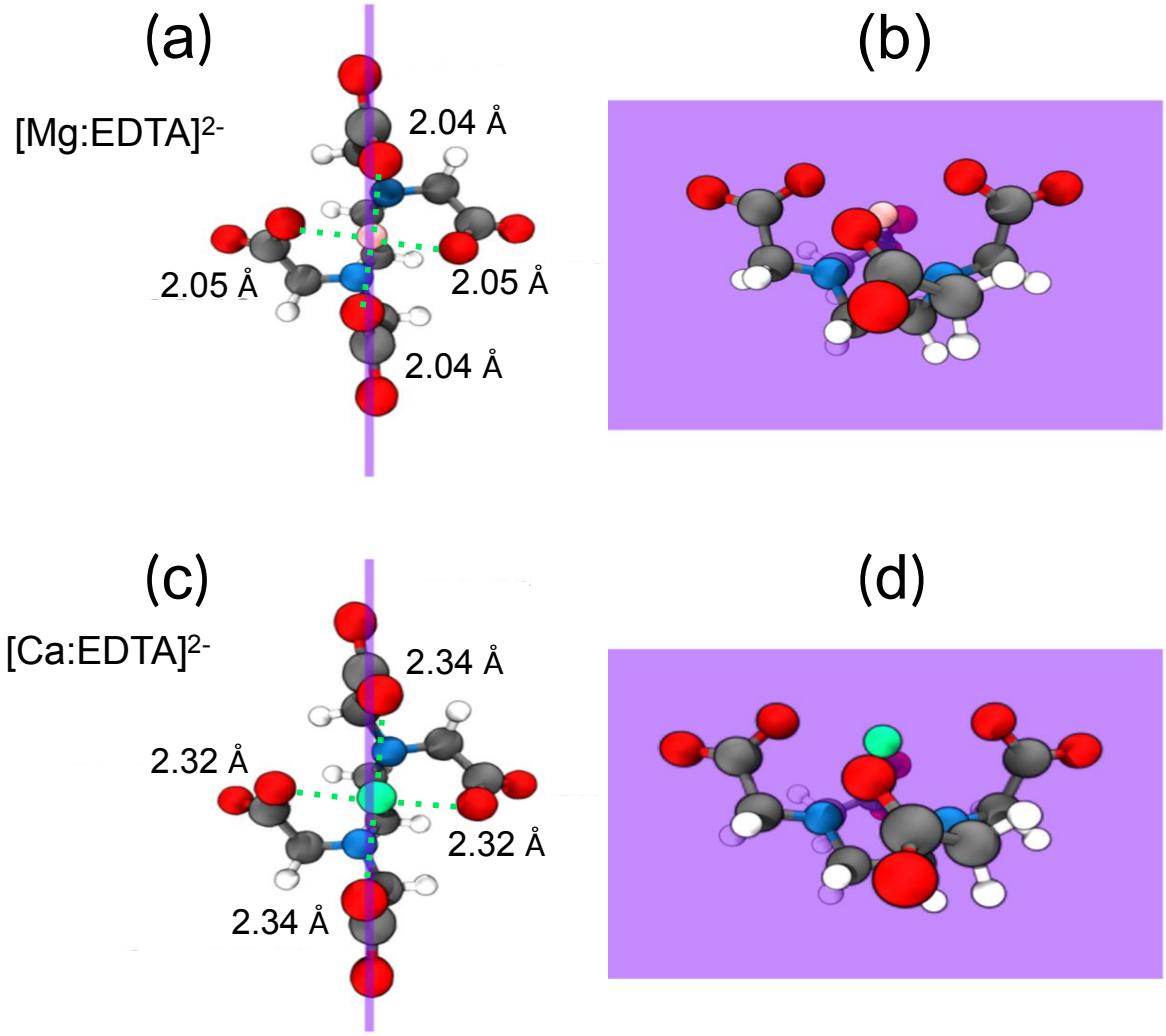

Figure 1: EDTA adopts an approximately C_2 symmetry when it binds Mg^{2+} (a, b) and Ca^{2+} (c, d). O–M^{2+} bond distances indicate a tighter binding geometry for $[Mg:EDTA]^{2-}$ than $[Ca:EDTA]^{2-}$. The sagittal acetates lie parallel to each other in a vertical plane (purple), while the other acetate pairs lie antiparallel to each other near the equator of the molecule.

and NMR[25] spectroscopies report the static structure and slower millisecond dynamics of ion binding.[26–28] The sub-picosecond temporal resolution of 2D-IR spectroscopy, however, can augment our understanding of the ultrafast dynamics in peptide–ion interactions.[21,29–34]

Infrared spectroscopy of EDTA probes the structure of carboxylate-Ca^{2+} ($[Ca{:}EDTA]^{2-}$) and carboxylate-Mg^{2+} ($[Mg{:}EDTA]^{2-}$) complexes.[11,14,16–18] Deacon and Phillips[35] empirically correlated the wavenumber difference between the antisymmetric stretch (COO^-_a) and symmetric stretch (COO^-_s) ($\Delta\nu_{a-s} = \nu_{COO^-_a} - \nu_{COO^-_s}$) with the binding geometry for aqueous metal acetato-carboxylate complexes. The $\Delta\nu_{a-s}$ roughly correlates to unidentate, bidentate, bridging, and pseudo-bridging binding types.[16,36,37] Later, however, Deacon and Phillips[38] noted the inadequacy of using the $\Delta\nu_{a-s}$ empirical relation to explain ion binding structures in multi-carboxylates. Complex multi-carboxylates' COO^-_s region exhibits additional features after metal binding,[1–3,16,18,20,21,36,39–43] whose origins were unexplained.

2D-IR spectroscopy of the COO^-_a promises insights into the local structure and dynamics of carboxylate groups. Because ions and molecules in the local solvation shell modulate the vibrational frequencies of carboxylate stretches, 2D-IR spectroscopy can report the picosecond structural dynamics. Metal coordination–induced geometry changes are reflected in the vibrational couplings. When a metal binds, the vibrations couple to generate cross-peaks in the 2D-IR spectrum. Coupling cross-peaks in EDTA and calmodulin (CaM) COO^-_a uncover structural changes.[18,19] The vibrations couple, through space (electrostatically) or mechanically (covalently), due to the metal binding event. Binding–induced structural changes have also been reported in the 2D-IR spectra of the amide modes in ionophores such as valinomycin[44] and ion channels.[33,45,46] For example, the side-on and end-on ion–pair conformers of calcium oxalate interconvert on a picosecond timescale.[47] A model Hamiltonian for the COO^-_a was able to relate the conformational changes due to oxalate–metal interaction to the spectral features of the COO^-_a vibration.[47–49] In trifluoroacetate, solvent fluctuations drive population relaxation from the pumped COO^-_a into the COO^-_s.[48]

Finally, the ion-coordination geometry and fluctuations in the binding pocket of wild

and mutated CaM were elucidated with 2D-IR spectroscopy.[18,20] Edington et al.[18,19] show that the COO^-_a reliably captures the ion–induced distortion in the binding geometry of EDTA and CaM. A comparison of Ca^{2+} and Ln^{3+} shows that the bound ion dictates if the CaM binding pocket will be compact and rigid or loose and flexible, which translates into downstream tertiary structural changes.[18] Separate active site mutations in CaM show different antisymmetric stretch cross-peak structures, which are the manifestations of the CaM binding pocket's conformational flexibility.[20] In each of these examples, the COO^-_a bands in 2D-IR spectra provided important insights into local structure and dynamics of these carboxylate moieties.

While investigation of the COO^-_a reveals some changes upon ion binding,[18–21,48] the symmetric stretch remains largely unexplored. Attenuated total reflection Fourier transform infrared (FTIR) spectroscopy shows that the COO^-_s can act as an indicator of transition metal ion binding in a self-assembled bilayer.[50] Donaldson et al.[51] probed the COO^-_s mode of a carboxylate-capped layer on gold nanoparticles to understand the correlation between the peptide-binding geometry and carboxylate orientation. Faint cross-peaks upon gold nanoparticle binding reflect the orientation of the carboxylates on the nanoparticle surface.

In part, the sparsity of studies using the symmetric stretch are due to the complex lineshape. The symmetric stretching band is complicated because the absorption frequencies of the COO^-_s mode and CH bending modes are similar. Absorption bands from the CH bending modes overlap with the COO^-_s band in EDTA in the absence of bound ions (apo-EDTA), making it challenging to separate their contributions.[19] As a result, the interpretation of features in the 1300–1500 cm^{-1} region is unclear, independent of metal ion binding.

The complexity of the COO^-_s band is also an opportunity. The substructures in the lineshape may reveal subtle conformational changes that the COO^-_a does not. We aim to connect the origin of the COO^-_s region vibrational structures to the metal–binding geometry of EDTA. We also explore the feasibility of utilizing the COO^-_s mode as a marker band for conformational changes in peptides.

We address the link between EDTA's COO_s^- IR spectral features and its binding conformation. Combining 2D-IR spectroscopy and density functional theory (DFT), we characterize the relationship between the vibrational spectrum of apo- and metal-bound EDTA and the geometry of binding. 2D-IR spectroscopy and DFT calculations show the impact of Ca^{2+} and Mg^{2+} binding in the COO_s^- region. To separate the contributions of the COO_s^- and CH bending modes in the 1000–1650 cm^{-1} region, we develop a scheme to calculate participation coefficients from the vibrational normal mode calculations. We use these participation coefficients to quantify the symmetric stretch and CH bending modes' local contribution to each normal mode and, from this information, assign the EDTA bands between 1000–1650 cm^{-1}. Furthermore, we apply energy decomposition analysis (EDA) methods to distinguish the different interaction energy terms that play a significant role in EDTA–ion binding. We use EDA to decipher the physically meaningful intermolecular interactions that initiate and drive the observed EDTA geometry changes upon metal binding.

This paper is organized as follows: First, we show the changes in the FTIR and 2D-IR spectra of EDTA as a function of the divalent ion identity (section 3.1). Next, to untangle the CH bending modes and COO_s^- contributions in the symmetric stretch region, we develop a participation coefficient analysis from DFT normal mode calculations. The participation coefficients help us assign the COO_s^- peaks (section 3.2). With those assignments, we rationalize the major differences in the 2D-IR spectra between the apo-EDTA, $[Ca:EDTA]^{2-}$, and $[Mg:EDTA]^{2-}$ COO_s^- and link them to the binding geometry of each ion (section 3.3). Finally, we use EDA calculations to fully characterize the nature of the intermolecular interactions that drive the transformation into the metal–bound conformation in EDTA (section 3.4).

2 Methods

2.1 Materials

Ultra pure grade $\geq 99.5\%$ tetra-sodium salt of EDTA ($C_{10}H_{12}N_2O_8Na_4{\cdot}H_2O$) was purchased from AMRESCO, Inc. Calcium chloride ($CaCl_2$) and magnesium chloride ($MgCl_2$) salts were obtained from Sigma-Aldrich, Inc. Deuterium oxide (D_2O) solution was bought from Cambridge Isotope Laboratories, Inc. Deuteration eliminates the overlap between the carboxylate stretch region and H_2O bending mode. To avoid metal contaminants from the glass surface containers via leaching,[52] EDTA solutions were made in 15 mL Falcon tubes. The powder form of EDTA and respective metal ions were directly mixed in D_2O to obtain the desired concentration. The uncorrected pH reading of the tetra-sodium EDTA salt was $\sim$11.2. FTIR spectroscopy (Figure 2) verified the complete deprotonation of the EDTA carboxylates in the aforementioned pH.

The 2D-IR samples were (1) 350 mM $[\text{apo-EDTA}]^{4-}$ in D_2O (2) 450 mM $[\text{Mg:EDTA}]^{2-}$ with 450 mM $MgCl_2$ in D_2O and (3) 460 mM $[\text{Ca:EDTA}]^{2-}$ with 460 mM $CaCl_2$ in D_2O solutions. These concentrations provided absorption in the 0.20–0.40 OD range for 2D-IR measurements.[53] Each FTIR and 2D-IR sample cell had a 15 µL solution droplet in between two 2 mm thick CaF_2 UV-grade windows separated by a 6 µm polytetrafluoroethylene spacer.

2.2 Linear IR

A Thermo Fisher Nicolet 6700 spectrometer recorded each sample's FTIR spectrum with $2\,\text{cm}^{-1}$ spectral resolution. The sample chamber was purged with nitrogen during data collection to eliminate water vapor.

2.3 2D-IR

A commercial, 5 kHz Ti:Sapphire laser (Coherent Legend Elite) generates $\sim$120 fs pulses of 805 nm light with $\sim$250 cm^{-1} full-width at half-maximum (FWHM) bandwidth and

1 mJ/pulse. An optical parametric amplifier generates mid-infrared pulses;[54] the amplified signal and idler pulses are mixed in a difference frequency mixing crystal, $AgGaS_2$, to generate 1.80 µJ/pulse at 1410 cm^{-1}.

The pump-probe geometry 2D-IR spectrometer is based on the design of Helbing et al.[55] The spectrometer generates two collinear pumps, a probe, and a reference pulse. A fast-scanning Mach-Zehnder interferometer generates the first coherence time, t_1, between the pumps. The population stage produces the waiting times, t_2, between the pump and the probe pulses. A Fourier transformation of the t_1 time at each t_2 gives the initial frequency axis, (ω_1). The signal field, which is self-heterodyned with the probe pulse, was diffracted by a 50 l/mm grating to disperse the ω_3 final frequencies.

A 2 × 32 mercury cadmium telluride detector (Infrared Associates, liquid N_2 cooled) collects the signal and reference. Signals are gated, integrated, digitized, and transferred to the computer using a Femtosecond Pulse Acquisition Spectrometer (Infrared Systems Development Corps.). MATLAB (MathWorks) is used to visualize and analyze the collected 2D-IR signal. In the current work, all the 2D-IR spectra are at t_2 = 200 fs with a signal averaging of ∼600 scans each and with resolutions of 6 cm^{-1} along ω_1 and 3 cm^{-1} along ω_3.

2.4 Calculations

2.4.1 Density functional theory

Geometry optimization and vibrational frequency calculations were performed on apo-EDTA (32 atoms) and $[Ca:EDTA]^{2-}$ and $[Mg:EDTA]^{2-}$ (33 atoms) with the M05-2X[56] and ωB97X-D[57,58] density functionals using a development version of Q-Chem.[59] All calculations use the def2-TZVP basis set. Standard grids 3 and 2, as implemented in Q-Chem,[60] were used for all M05-2X and ωB97X-D calculations respectively. The condensed phase environment was incorporated via the SMD[61] implicit polarizable continuum solvation model for all three molecules. The three molecules were generated in Avogadro[62] with an initial force-field based geometry optimization (MMFF94s with steepest descent), from which the resulting

Cartesian coordinates were used as input to the DFT geometry optimizations. ChElPG-based atomic partial charges of the metal-bound Mg^{2+} and Ca^{2+} were performed on the optimized structures. Computed frequencies used in the paper are unscaled, and the scaling factors with their respective scaled frequencies were calculated for both functionals (Supporting Information).

The M05-2X functional was chosen because it accurately represents carboxylate systems, especially for thermodynamic information.[63,64] The remaining differences between computed and experimental spectra generally originate from incomplete treatment of the condensed phase environment[65,66] and anharmonicity. More specifically, gas-phase single-conformer calculations are missing solute-solvent interactions and contributions from energetically low-lying conformers. We approximate the solute-solvent interactions using an implicit solvent model in order to avoid the costly sampling required for incorporating explicit solvation. Currently, a test set of small molecules, such as acetate and citrate, are used to benchmark carboxylate spectra at the comparable M05-2X/cc-pVTZ/SMD level of theory,[64] but these small benchmarks may still not consider the complicated interactions of molecules as large as EDTA; for example, the M05-2X functional is reported to overestimate the COO^- symmetric stretch frequencies compared to experiment. As comparison, we supplement the use of the M05-2X functional with ωB97X-D, since previous work[67,68] shows similarities between the two functionals for harmonic frequencies.

2.4.2 Intermolecular interactions

To further understand the nature of the metal-ligand binding, we quantified this intermolecular interaction using EDA based on absolutely localized molecular orbitals (ALMO-EDA), which quantifies the interaction based on physically intuitive components. In ALMO-EDA with implicit solvent, the total change in energy due to bringing isolated fragments together is

given by

$$\Delta E_{\text{int}}^{(\text{s})} = \Delta E_{\text{geom}}^{(\text{s})} + \Delta E_{\text{frz}}^{(\text{s})} + \Delta E_{\text{pol}}^{(\text{s})} + \Delta E_{\text{CT}}^{(\text{s})} \tag{1}$$

$$= \Delta E_{\text{geom}}^{(\text{s})} + \left(\Delta E_{\text{elec}}^{(\text{s})} + \Delta E_{\text{Pauli}}^{(\text{s})} + \Delta E_{\text{disp}}^{(\text{s})}\right) + \Delta E_{\text{pol}}^{(\text{s})} + \Delta E_{\text{CT}}^{(\text{s})}, \tag{2}$$

where ΔE_{geom} is the energy increase caused by the fragments adopting their interacting geometries, ΔE_{frz} is the energy change from bringing fragments together into the final supermolecular geometry while keeping their densities frozen and not allowing them to relax, ΔE_{pol} is the energy lowering from allowing intrafragment density relaxation in the presence of other fragments while disallowing interfragment charge flow, and ΔE_{CT} corresponds to the charge transfer caused by lifting this last restriction. The frozen density term can be further broken down into three primary parts: ΔE_{elec} is the electrostatic Coulomb interaction between isolated fragments, ΔE_{disp} is the dispersion interaction, and ΔE_{Pauli} is the remaining short-ranged non-electrostatic components of bringing fragments together while keeping their densities constrained. The superscript "(s)" signifies that a term includes solvent effects.

The ALMO-EDA formalism is based on the classical decomposition of the frozen density[69,70] with solvation[71] as implemented in Q-Chem. As validation, we also performed symmetry-adapted perturbation theory (SAPT) calculations, which originate from a different theoretical foundation but contains comparable terms. These calculations are based on the SAPT0 formulation[72,73] as implemented in Psi4.[74] All ALMO-EDA and SAPT calculations used the same geometries as the ωB97X-D/def2-TZVP/SMD frequency calculations. ALMO-EDA uses this method chemistry for all fragment wavefunctions, including the solvent model. SAPT instead starts from a Hartree–Fock reference. Due to technical problems with including solvation, all SAPT calculations were performed in the gas phase. However, we see that trends in like terms between ALMO-EDA and SAPT are qualitatively similar (vide infra). To better compare against ALMO-EDA, monomer-basis SAPT results will be presented in the main text, and dimer-basis SAPT results are in the Supporting Information. In order to

perform this comparison, we modify equation 1 slightly to

$$\Delta E_{\text{int}} = \Delta E^{(\text{s})}_{\text{geom}} + \Delta E^{\text{cls}(0)}_{\text{elec}} + \Delta E^{\text{el}}_{\text{solv}} + \Delta E^{\text{mod(s)}}_{\text{Pauli}} + \Delta E^{(\text{s})}_{\text{disp}} + \Delta E^{(\text{s})}_{\text{pol}} + \Delta E^{(\text{s})}_{\text{CT}} \tag{3}$$

$$= \Delta E_{\text{geom}} + \Delta E_{\text{elec}} + \Delta E_{\text{solv}} + \Delta E_{\text{Pauli}} + \Delta E_{\text{disp}} + \Delta E_{\text{pol}} + \Delta E_{\text{CT}}, \tag{4}$$

where the classical decomposition is applied and the solvent correction to the electrostatic interaction is considered separately (see equation 9 in ref. 71). The superscript "(0)" indicates the term is calculated without solvent effects.

2.4.3 Participation coefficients

Participation coefficients P were calculated to determine the contribution of CHH and COO motions to the normal modes of the apo- and complexed forms of EDTA. In general, P is the square of the overlap of a unit basis vector on the EDTA molecule (apo or complex) normal mode vector in the subspace of a set of atoms for the molecule. The participation coefficients can be represented generally by:

$$P_{i,j} = \frac{\left| \langle {}_{basis}\vec{\nu}_i | {}_{mol}\vec{\nu}_j \rangle \right|^2}{\langle {}_{basis}\vec{\nu}_i | {}_{basis}\vec{\nu}_i \rangle}. \tag{5}$$

${}_{basis}\vec{\nu}_i$ and ${}_{mol}\vec{\nu}_j$ refer to the i-th basis normal mode (we will discuss our notion of basis shortly) and the j-th molecule normal mode (determined from the frequency calculations described in the previous section), respectively. For our purposes, $P_{i,j}$ will always be calculated for a subspace of the full nuclear position coordinates of the molecule. The subspace of coordinates will always consist of the carboxylate COO atom positions or the terminal CHH atom positions of a specified acetate group on EDTA. Note that only the basis vector in the subspace of atoms is normalized, and hence the participation coefficient is bounded by the square length of the normal mode in the subspace of the specified CHH or COO coordinates (eq. 6). If index l spans this subset of nuclear position coordinates, S, then we can express

this bound as

$$P_{i,j} \leq \sum_{l \in S} {}_{mol}\nu_{jl}{}^2, \tag{6}$$

where j and i are defined as above.

We were particularly interested in calculating participation coefficients for the carboxylate regions ($S = \mathrm{COO}$) and the alpha carbon regions ($S = \mathrm{CHH}$) in the EDTA molecules since CHH motions tend to couple with COO symmetric stretch regions. The basis vectors for these two regions were created according to the following procedure. We desired a complete basis to fully describe the motion of these atoms as they contribute to the overall normal modes. To this end, we created orientation-dependent rotation and translation normal modes in the subspace of the CHH or COO atoms for each of the four acetates in each molecule. Since the equilibrium positions for the three atoms specify a plane, the normal to this plane specifies one of the basis vectors used to create the rotation and translation normal modes. The midpoint bisector (drawn from the carbon atom to the midpoint between the two hydrogen/oxygen atom positions) in the CHH/COO plane was used as the second basis vector, and the cross product of the the previous two basis vectors determined the third basis vector. Given the normalized basis vector $\vec{e}_i$, the corresponding normalized mass weighted translation vector (for a CHH group as an example), $\mathbf{T}_i$, is

$$\mathbf{T}_i = \frac{(\sqrt{m_C} \cdot \vec{e}_i, \sqrt{m_{H_1}} \cdot \vec{e}_i, \sqrt{m_{H_2}} \cdot \vec{e}_i)}{(\sqrt{m_C + m_{H_1} + m_{H_2}})}. \tag{7}$$

For the rotational vectors, the moment of inertia tensor, $\mathbf{I}$, was calculated for the CHH and COO atoms of each acetate using the positions relative to the center of mass of the three atom system, and the tensor was diagonalized to yield the three angular velocity vectors (eigenvectors), $\vec{\omega}_i$. These vectors were ordered by their maximal overlap with the three translational basis vectors $\vec{e}_i$ given above. The normalized mass weighted rotational vectors

(for a CHH group as an example) are then given by

$$\mathbf{R}_i = \frac{(\sqrt{m_C} \cdot \vec{r}_C \times \vec{\omega}_i, \sqrt{m_{H_1}} \cdot \vec{r}_{H_1} \times \vec{\omega}_i, \sqrt{m_{H_2}} \cdot \vec{r}_{H_2} \times \vec{\omega}_i)}{\sqrt{(\omega_i)}}, \tag{8}$$

where ω_i is the corresponding eigenvalue to the eigenvector of the moment of inertia tensor. Note that the coordinates $\vec{r}$ here are given relative to the center of mass ("com") of the three atoms (e.g., $\vec{r}_C = \vec{x}_C - \vec{r}_{\text{com}}$).

The vibrations were determined from the diagonalization of the mass weighted Hessian for the toy harmonic potential given in equations 9 and 10 and were ordered by eigenvalue:

$$E = k_{CH/CO} \sum_{i,j \subset S} (|\vec{r}_i - \vec{r}_j| - r_{ij}^0)^2 + k_{\angle CHH/COO}(\theta - \theta^0)^2 \tag{9}$$

where θ is defined as:

$$\theta = \arccos\left(\frac{(\vec{r}_{H_1} - \vec{r}_C) \cdot (\vec{r}_{H_2} - \vec{r}_C)}{|\vec{r}_{H_1} - \vec{r}_C||\vec{r}_{H_2} - \vec{r}_C|}\right). \tag{10}$$

$k_{CH/CO}$ is the force constant of the CH/CO bond, while $k_{\angle CHH/COO}$ is the force constant for the H-C-H/O-C-O angle. Since only the relative values for these force constants are important, DFT calculations on methane (see supporting information) indicate that the spring constant for the C-H stretch is about 4 times that of the HCH bend force constant, and so $k_{CH/CO} = 4$ and $k_{\angle CHH/COO} = 1$ were chosen for the model potential. (The value $k_{CH/CO} = 4$ was determined crudely from the DFT calculations for methane from the frequencies, f and reduced masses m to determine $k_{CH/CO} = \frac{k_{stretch}}{k_{freq}}$ from $\frac{f_{stretch}}{f_{bend}} = \sqrt{\frac{k_{stretch} m_{bend}}{k_{bend} m_{stretch}}}$). $\vec{r_i}$ and $\vec{r_j}$ correspond to the position of the i^{th} and j^{th} atoms. r_{ij}^0 is the equilibrium bond distance between the pair of atoms i and j. S is the set of pairs of atoms that are bonded to one another. θ is calculated from equation 10 as the angle between $\text{H}_1 - \text{C} - \text{H}_2$, where $\vec{r}_{\text{H}_1}$, $\vec{r}_{\text{H}_2}$, and $\vec{r}_{\text{C}}$ are the positions of H_1, H_2 and C. Here r^0 and θ^0 are the equilibrium position and angles. The resulting 9 basis vectors form a complete and orthonormal basis in this subspace.

3 Results and Discussion

3.1 Carboxylate stretch infrared peaks in apo-EDTA change shape after metal binding

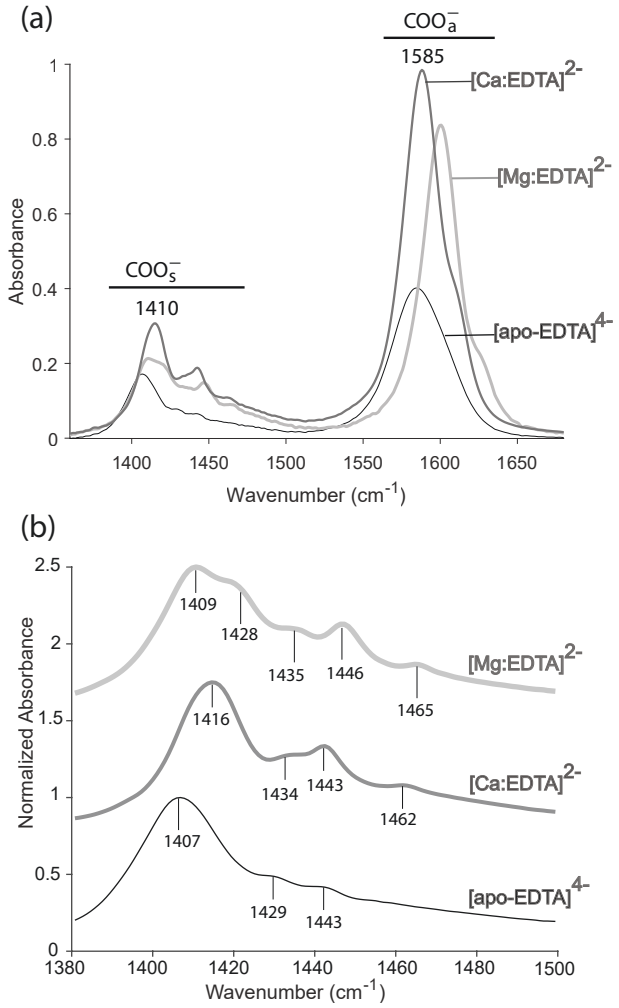

Figure 2: (a) FTIR spectra of apo-EDTA, $[Ca:EDTA]^{2-}$, and $[Mg:EDTA]^{2-}$ reveal the frequency, structure and lineshape changes in the COO^- stretch region. (b) The normalized spectra of the COO_s^- region have the peaks labeled for the three molecules (offsets: $[Mg:EDTA]^{2-}$ 1.50 A.U. and $[Ca:EDTA]^{2-}$ 0.75 A.U.)

Carboxylates absorb in the 1300–1700 cm^{-1} region (Figure 2). In apo-EDTA, the COO_a^- absorbs twice as strongly as the COO_s^-. The COO_a^- (1585 cm^{-1}) has a broad, roughly Gaussian peak shape (44 cm^{-1} FWHM), which agrees with literature.[13,40] The COO_s^- (1410 cm^{-1}) band,

on the other hand, is broad (∼42 cm^{-1} FWHM) and asymmetrical (absorption extends to nearly 1500 cm^{-1}). On top of the broad COO_s^- peak are lower intensity peaks at 1429 cm^{-1} and 1443 cm^{-1}, as previously observed.[13,14,36]

When EDTA binds Ca^{2+} or Mg^{2+}, the carboxylate stretches change their peak positions, structures, and lineshapes[13,14,36] (Figure 2). In the metal–bound EDTA, the COO_a^- band narrows to a Lorenzian ($[Ca:EDTA]^{2-}$: 31 cm^{-1} FWHM, $[Mg:EDTA]^{2-}$: 29 cm^{-1} FWHM), with a shoulder on the high frequency side.[19] The COO_s^- band blueshifts to 1416 cm^{-1} in $[Ca:EDTA]^{2-}$ and to 1409 cm^{-1} in $[Mg:EDTA]^{2-}$. In $[Ca:EDTA]^{2-}$, three new peaks grow at 1434 cm^{-1}, 1443 cm^{-1}, and 1462 cm^{-1}, while in $[Mg:EDTA]^{2-}$, four new peaks appear after complexation (1428 cm^{-1}, 1435 cm^{-1}, 1446 cm^{-1}, 1465 cm^{-1}).

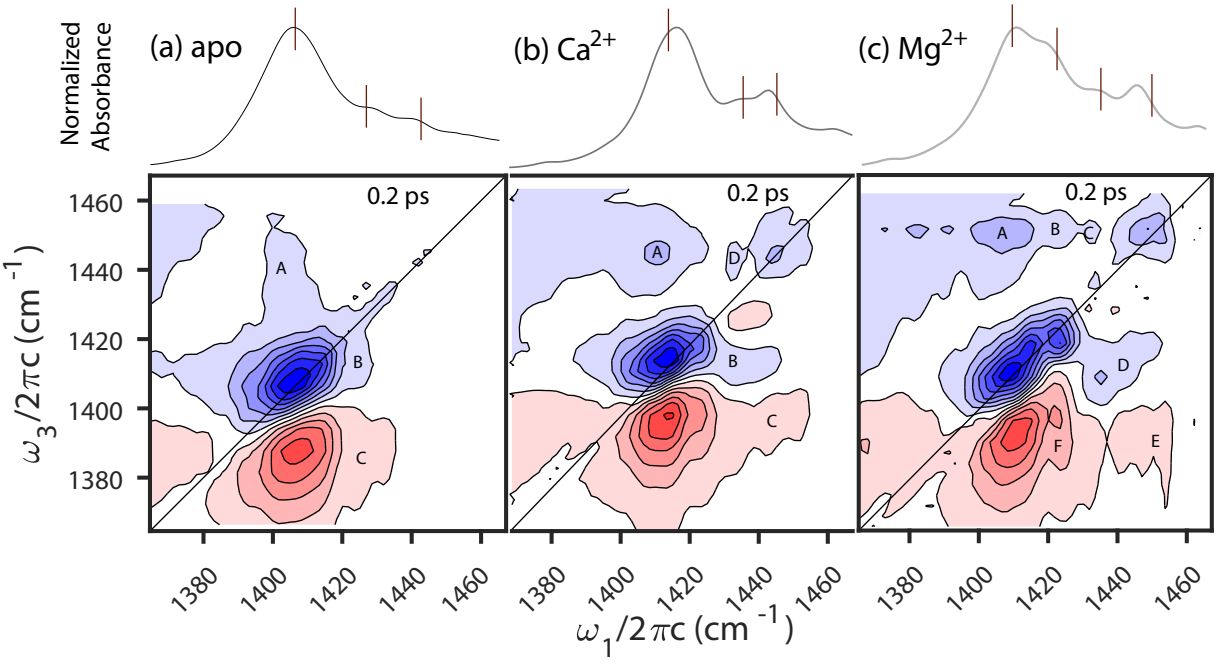

Figure 3: 2D-IR at t_2 = 200 fs spectra show the diagonal and cross-peaks in the three molecules' COO_s^- region: (a) 350 mM apo-EDTA (b) 460 mM $[Ca:EDTA]^{2-}$ (c) 450 mM $[Mg:EDTA]^{2-}$. For all three molecules, the bottom 2D-IR panel has cross-peak features labeled in the blue and red lobes. The top panel is the normalized FTIR spectrum of each molecule with peak centers aligned to the respective 2D-IR center frequencies.

2D-IR spectra add additional information about the coupling between the COO_s bands. At the earliest waiting time (t_2 = 200 fs), both diagonal and cross-peaks appear in the

COO_s^- region of the 2D-IR spectrum of apo-EDTA (Figure 3 (a)). The diagonal peak $\omega_1 = \omega_3 = 1407\,\mathrm{cm}^{-1}$ is inhomogeneously broadened, stretches along the diagonal, and has an elliptical shape. Faint diagonal peaks appear at $\omega_1 = 1429\,\mathrm{cm}^{-1}$ and $\omega_1 = 1443\,\mathrm{cm}^{-1}$. In addition to the diagonal band, a negative cross-peak, A, at $\omega_1 = 1407\,\mathrm{cm}^{-1}$ stretches from $\omega_3 = 1423$–$1450\,\mathrm{cm}^{-1}$, a negative cross-peak, B, ($\omega_1 = 1423\,\mathrm{cm}^{-1}$) spans from $\omega_3 = 1407$–$1420\,\mathrm{cm}^{-1}$, and a positive cross-peak, C, stretches from $\omega_3 = 1380$–$1400\,\mathrm{cm}^{-1}$.

The 2D-IR spectrum of the COO_s^- vibrations changes upon metal binding to EDTA (Figure 3). At the earliest waiting time ($t_2 = 200\,\mathrm{fs}$), new diagonal bands and cross-peaks become apparent after metal binding. Consistent with the FTIR spectra, three diagonal bands in $[\mathrm{Ca{:}EDTA}]^{2-}$ and four in $[\mathrm{Mg{:}EDTA}]^{2-}$ are apparent. Additionally, the broad cross-peaks in apo-EDTA (A-C) resolve into sharp features in $[\mathrm{Ca{:}EDTA}]^{2-}$ (A-D) and $[\mathrm{Mg{:}EDTA}]^{2-}$ (A-F).

Our objective is to understand the origin of these vibrational bands in the FTIR and 2D-IR spectra after Ca^{2+} and Mg^{2+} ions bind to EDTA. In the following section, we will assign the vibrational bands utilizing the participation coefficients.

3.2 COO_s^-, CH_s and CH_w mix in apo-EDTA and its complexes

In this section, the entire 1000–$1630\,\mathrm{cm}^{-1}$ range is assigned. We will first walk through the assignment of the COO_a^- band using the participation coefficient method, which will assist our understanding of the mixed COO_s^- assignments. Finally, we will discuss the nuances in the spectra of the three molecules. We will also address some of the unresolved assignments seen in the literature.

The calculated COO participation coefficients show the contribution of the idealized carboxylate vibrations to the normal modes of EDTA and the metal complexes for symmetric (Figure 4a) and antisymmetric (Figure 4b) stretches. In each panel, the x-axis indices are the normal modes from the respective three molecules (Table Supporting Information) and the y-axis indices (1–4) are the four acetate groups in EDTA. In apo-EDTA (Figure 4b, top), only

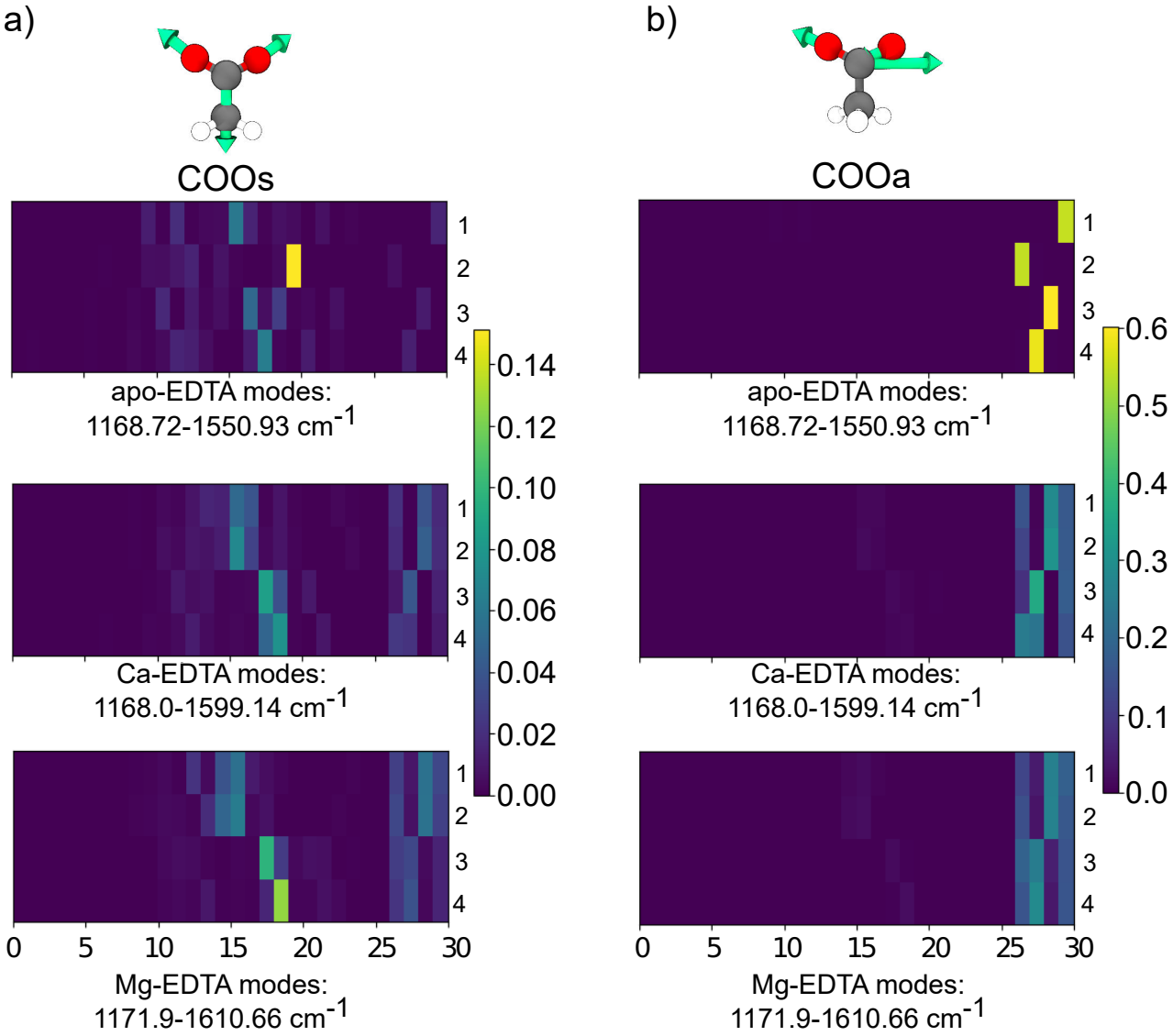

Figure 4: Participation coefficients for the COO_a^- are higher than the COO_s^-. Each column in the COO plot shows that COO_s^- is spread across more than four normal modes, unlike the COO_a^- which is limited to four modes. The top panel is apo-EDTA, $[Ca:EDTA]^{2-}$ is the mid-panel, and the bottom panel is $[Mg:EDTA]^{2-}$. The frequency range and indices are consistent throughout the paper. The left and right columns are COO_s^- and COO_a^- participation respectively. 1 and 2 are the sagittal acetates and the equatorial acetates are 3 and 4. All scales can be converted to a percent participation by multiplying with a factor of 100.

the normal modes 26–29 have appreciable projection onto the idealized COO^-_a modes. In addition, each of these normal modes projects only onto one of the localized COO^-_a stretches, which shows that the vibrations are localized in apo-EDTA. In $[Ca{:}EDTA]^{2-}$ (Figure 4b, middle), the COO^-_a participation coefficients also indicate that only normal modes 26–29 have appreciable COO^-_a character. The normal modes each project onto several of the idealized COO^-_a vibrations, however, indicating that the normal modes are delocalized across several carboxylates. In $[Mg{:}EDTA]^{2-}$ (Figure 4b, bottom), the same general patterns emerge, and modes 27 and 28 each are nearly equally delocalized across a pair of carboxylates. We will return to the structural origin of this observation later in this section. In summary, the participation coefficients show the projection of each normal mode onto an idealized basis vector, which can quantitatively illuminate the character of the normal mode and its degree of delocalization. In this case, we observe that only four normal modes have COO^-_a character, and metal binding can induce delocalization of the vibrations, as expected.[19]

Having introduced the relatively straightforward COO^-_a modes, we turn now to the COO^-_s modes, which are more complicated. In the COO^-_s of apo-EDTA (Figure 4a, top), more than four normal modes project onto the idealized COO^-_s vibration. The participation coefficients are appreciable from modes 10–19, indicating that the ideal symmetric stretch vibration is present in all these modes, while modes 15–19 overlap the most. In both $[Ca{:}EDTA]^{2-}$ and $[Mg{:}EDTA]^{2-}$ (Figure 4a, middle and bottom), modes 14–18 overlap the most with the idealized COO^-_s vibration. Some contribution of modes > 25 is noted, which we attribute to the lower symmetry of each carboxylate upon ion binding, i.e., symmetric and antisymmetric are no longer rigorous symmetry labels because of the nearby ion. Even with this complication, the participation coefficients allow us to identify normal modes 14–18 as the primary carboxylate symmetric stretches in EDTA and its metal complexes.

The COO^-_s motions are mostly localized, independent of metal binding (Figure 4a). The mixed COO^-_s are localized to each carboxylate. The highest participation from one COO^-_s in the $1464\,cm^{-1}$ calculated band is $\sim$15%, and for the rest of the individual COO^-_s modes

it is ∼7%. With Ca^{2+} binding, the highest COO_s^- participation redistributes from 7 to 9%, whereas in Mg^{2+} the individual COO_s^- participation falls in a broad range from 3–13%. The carboxylates, however, (Figure 4a) participate alone (modes 14–18), implying that only one carboxylate is heavily involved in the symmetric stretch vibration. Metal binding more or less does not change the localization of the COO_s^- vibration. We interpret that the insignificant delocalization in the metal complexes is from their low C_2 symmetry, while the disordered apo-EDTA structure produces localized motions. We will examine how the structure of the EDTA affects the 2D-IR spectra in-depth in the next section (Section 3.3).

Projecting the normal modes of apo- and complexed EDTA onto the idealized acetate CHH normal modes (twist (CH_t), wag (CH_w), and scissor (CH_s)) reveal their contribution in the 1000–1650 cm^{-1} region (Figure 5). In the CHH participation coefficients, two rows of information are available for each of the twist, wag, and scissor motions. For each of them, the top row, labeled Avg, includes the mean participation from all four CHH proximal to the carboxylates, whereas the four rows below the average show the participation of each of these four terminal CHH for CH_t (top panels), CH_w (middle panels), and CH_s (bottom panels), respectively.

The CHH participation plots first allow us to identify which normal modes contain significant contributions of CH bending character. In apo-EDTA the CH_t mode is confined to the indices 0–9 (Figure 5a, top), the CH_w mode is mostly prominent in the 9–19 modes (Figure 5a, middle), and the CH_s vibration appears most strongly in modes 15–24 (Figure 5a, middle). The same trend holds independent of metal binding (Figure 5b, c).

For COO_a^- normal modes, the CHH participation coefficients show that they have minimal overlap with the CH_t, CH_w, and CH_s vibrations in the three molecules. Looking at indices 26–29 of apo-EDTA, we see only a minimal overlap of the CH_w modes ($< 15\%$) (Figure 5a, top) with the normal modes of the COO_a^- vibrations; the CH_t (Figure 5a, middle) and CH_s (Figure 5a, bottom) normal modes overlap even less ($< 1\%$). Similarly, in both $[Ca{:}EDTA]^{2-}$ (Figure 5b) and $[Mg{:}EDTA]^{2-}$ (Figure 5c), modes 26–29 have an insignificant contribution

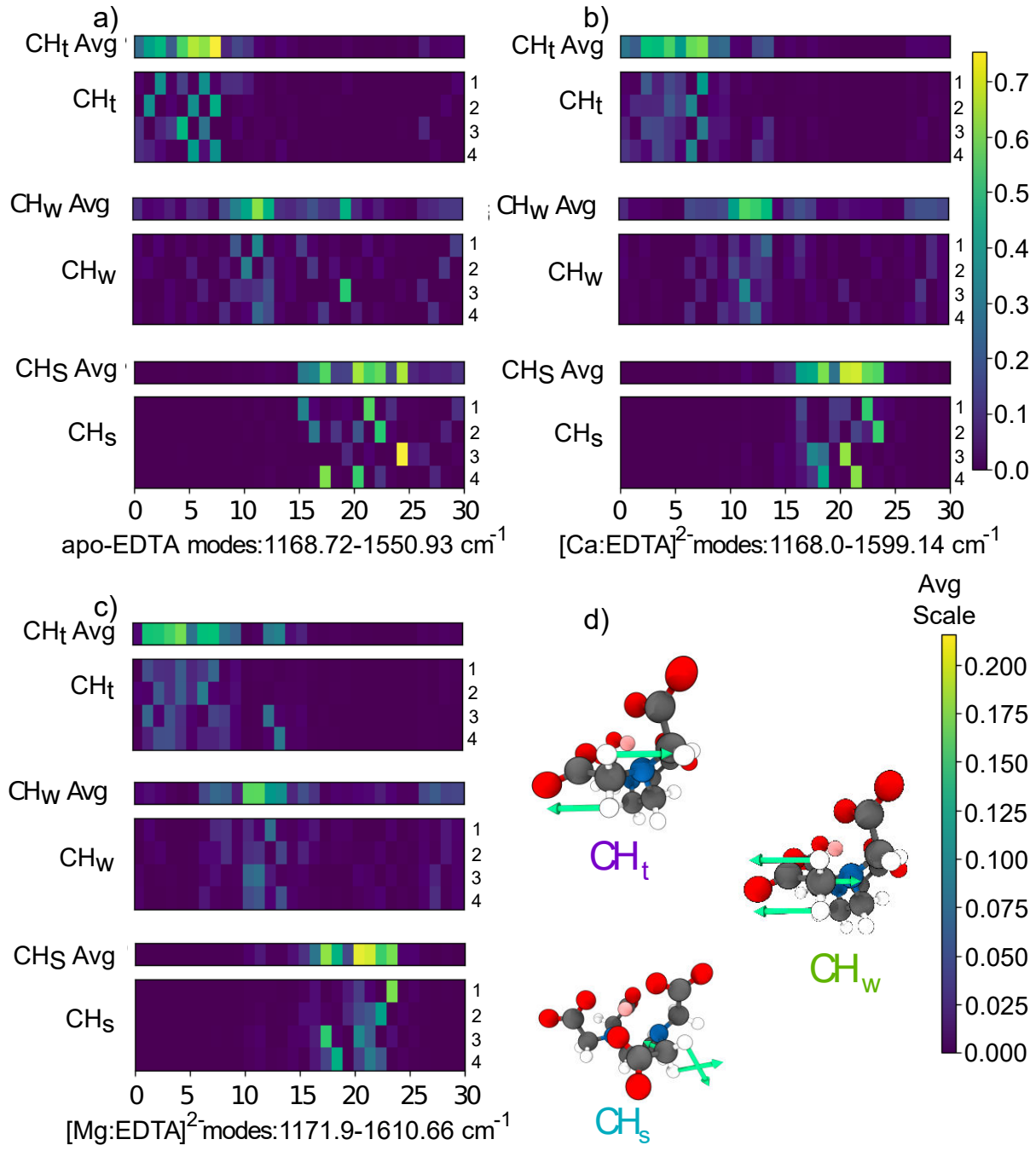

Figure 5: Contribution from the CH_t, CH_w, and CH_s modes to individual modes in the (a) apo-EDTA, (b) $[Ca:EDTA]^{2-}$, and (c) $[Mg:EDTA]^{2-}$ molecules differs. Averages for the four terminal acetate CHH are shown above the respective participation plots for CH_t, CH_w, and CH_s. 1 and 2 are the sagittal acetates, while 3 and 4 are the equatorial acetates. The scales can be converted to percent participation by multiplying with a factor of 100. The CH_t, CH_w, and CH_s motions are shown in (d).

from the CHH participation coefficients. This shows that even in the complexed form, the COO_a^- do not mix with the CH_t, CH_w, and CH_s vibrations.

For COO_s^- normal modes, on the other hand, the CHH participation plots show significant mixing of the COO_s^- modes and the CH motions, especially CH_s modes. Modes 14–18 of apo-EDTA elucidate the prominent CHH participation projection in these normal modes. This region in apo-EDTA, which describes the majority of COO_s^- motion, has significant projections (∼33–63%) from the ideal CH_s modes (Figure 5a, bottom) and minor contribution (∼ 16%) from the ideal CH_w modes (Figure 5a, middle). From these observations, we infer that the COO_s^- mixes both with the CH_s and the CH_w vibrations. We also observe that the CH_s modes project only onto one of the CHH near the carboxylates, reflecting the localized character of these modes. Similarly, in $[Ca:EDTA]^{2-}$ and $[Mg:EDTA]^{2-}$, the COO_s^- modes mix more with the CH_s than with the CH_w modes. Therefore, we conclude that after complexation the COO_s^- mixes more with the CH_s modes (∼45%) than the CH_w modes (<10%).

The participation coefficients allow assignments of the observed features in the linear absorption spectrum (Figure 6). The left column shows all the normal modes as stick spectra and with $8\,cm^{-1}$ Gaussian broadening. Modes 0–30 are assigned based on the participation coefficients. The right column presents the COO_s region (1400–1550 cm^{-1}) overlaid with the experimental absorption spectra. The wavenumber axes are shifted to accommodate the differences.

In the COO_s region (Figure 6b), apo-EDTA's three main peak features are the mixed COO_s^-, CH_w, and CH_s modes. The five symmetric stretches are clustered within the main peak, A (1407 cm^{-1}). The most intense COO_s^- peak (mode 16), is a carboxylate stretch with participation from scissor modes. The remaining three modes are mixed with CH_w and CH_s modes. Peak B (1429 cm^{-1}) encompasses the modes 20 and 21, which are CH_s motions. Band C (1443 cm^{-1}) corresponds most closely to the CH_s vibration in modes 22 and 23. The broad and asymmetric line profile of the COO_s^- band in apo-EDTA results from the low intensity

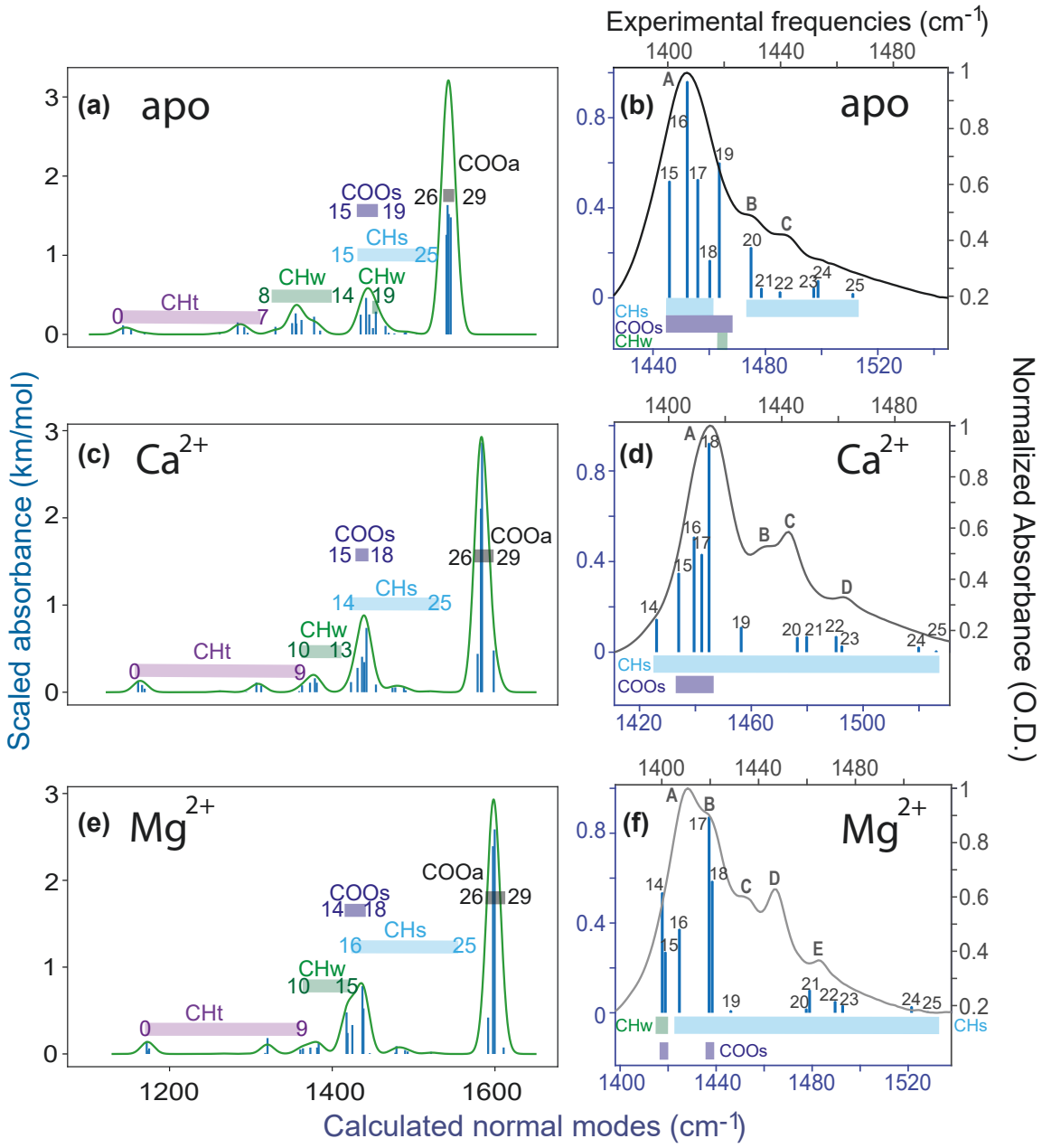

Figure 6: Indices 0–9 are CH_t vibration, indices ~10–15 are CH_w modes, the 16–25 region constitutes the CH_s modes, and the COO_a^- modes are indices 26–29. The COO_s^- vibrations fall within the CH_s frequencies. The three rows represent the three molecules, the left column shows the normal modes and the experimental COO_s^- overlays the same normal mode region in the right column. Apo-EDTA is the top row((a), (b)), $[Ca:EDTA]^{2-}$ is middle row ((c) and (d)), and $[Mg:EDTA]^{2-}$ is the bottom row ((e), (f)). Spectra shown here are calculated with M05-2X/def2-TZVP/SMD theory, Gaussian width = 8 cm^{-1}, intensity scaling factor = 0.0015, and 1000–1650 cm^{-1}.

Table 1: Normal mode assignment from M05-2X participation coefficient (pc) analyses in apo-EDTA, $[Ca:EDTA]^{2-}$, $[Mg:EDTA]^{2-}$ molecules for $1000–1650\,cm^{-1}$ range.

pc index	Calculated frequency (cm^{-1})	Predominant vibration
	$[apo\text{-}EDTA]^{4-}$	
0–7	1169–1314	CH_t
8–14, 19	1346–1399, 1464	CH_w
15–18, 20–25	1446–1460, 1475–1511	CH_s
15–19	1446–1464	COO_s
26–29	1546–1551	COO_a
	$[Ca:EDTA]^{2-}$	
0–9	1168–1363	CH_t
10–13	1367–1385	CH_w
14–25	1426–1526	CH_s
15–18	1434–1445	COO_s
26–29	1580–1599	COO_a
	$[Mg:EDTA]^{2-}$	
0–9	1172–1361	CH_t
10–15	1364–1419	CH_w
16–25	1425–1528	CH_s
14–15, 17–18	1418–1438	COO_s
26–29	1592–1611	COO_a

scissor motions in the modes 24 and 25 (Figure 6a, b). The relative IR intensity of these scissor modes are at most 20% of the mixed COO_s^- modes. We expect, based on the 2D-IR lineshapes, that disorder in the solvent broadens the frequency distribution for these scissor modes.

The absorption features of the $[Ca:EDTA]^{2-}$ symmetric stretch region are composed of COO_s^- and CH_s modes (Figures 6d). The main band, A ($1416\,cm^{-1}$), contains all the COO_s^- normal modes (modes 15–18). We assign the absorption band B ($1434\,cm^{-1}$) to CH_s vibrations (modes 20 and 21). We assign absorption bands C and D ($1443\,cm^{-1}$ and $1462\,cm^{-1}$) to pairs of CH_s stretches (modes 22 and 23 and modes 24 and 25, respectively).

Alternatively, the absorption band at $1434\,cm^{-1}$ (peak B) could be mode 19 (Figures 6d). We disfavor this assignment because mode 19 is an out-of-plane rotation motion of the ethylene CHH and the terminal CHH in the sagittal plane, while modes 20 and 21 are the in-phase and out-of-phase CH_s vibrations of all the terminal CHH, respectively. In the CHH participation coefficients, modes 19, 20, and 21 have participation from the terminal sagittal CH_s (Figure 5b rows 1 and 2), which indicates that these terminal atoms contribute to the three normal modes. Taken together, the calculated IR intensity and the CHH participation coefficients of modes 20 and 21 are stronger than mode 19 (Figures 6d and 5b). Furthermore, the ωB97X-D calculation reveals that mode 19 lies within the bandshape A ($1416\,cm^{-1}$) (Supporting Information). Thus, the peak B is more likely modes 20 and 21 rather than mode 19.

In the $[Mg:EDTA]^{2-}$ symmetric stretching region, two of the peaks are groups of COO_s^- modes and the remaining bands are CH_s modes (Figures 6f). The peak A ($1409\,cm^{-1}$) envelopes the normal modes 14, 15, and 16. Modes 14 and 15 are the symmetric stretch vibrations from the sagittal carboxylates and have participation from CH_w vibration, while mode 16 is primarily a CH_s motion. The absorption peak B ($1428\,cm^{-1}$) consists of the COO_s^- and CH_s vibrations (modes 17, 18) from the equatorial carboxylates. Mode 19 is a CH_s vibration that overlaps peak B. The remaining peaks in the linear spectrum (C, D, and

E) are assigned to modes 20 and 21, modes 22 and 23, and modes 24 and 25, respectively. All these modes 20–25 are CH_s vibrations (Figure 6f).

The observed IR spectrum and the calculated mode mixing in $[Ca:EDTA]^{2-}$ and $[Mg:EDTA]^{2-}$ are a result of the binding geometry. In both $[Ca:EDTA]^{2-}$ and $[Mg:EDTA]^{2-}$, the sagittal carboxylate pair (Ca^{2+} modes 15 and 16; Mg^{2+} modes 14 and 15) is further redshifted than the equatorial pair of carboxylates (Ca^{2+} and Mg^{2+}modes 17 and 18). The difference in the frequency of these vibrations depends on the placement of the metal in the EDTA binding pocket. In $[Mg:EDTA]^{2-}$, the sagittal and equatorial COO_s modes have a greater difference in frequency causing two peaks at $1409\,cm^{-1}$ and $1428\,cm^{-1}$ (A and B) to be observed (Figure 6d); in $[Ca:EDTA]^{2-}$, the sagittal and equatorial COO_s modes are more similar and only one broad absorption band A is observed (Figure 6f).

To determine the effect of geometrical distortion on the infrared spectra, we performed another set of DFT calculations where we first optimized geometry with the Mg^{2+} or Ca^{2+} ion and then removed the metal keeping the deformed geometry intact. In the deformed geometries, the calculated normal modes show the same trend – splitting in the Mg^{2+}-bound geometry and no splitting in the Ca^{2+}-bound geometry – even without the presence of the metal. This result strongly suggests that the geometrical deformation is responsible for the greater splitting between sagittal and equatorial COO_s^- modes in $[Mg:EDTA]^{2-}$ than in $[Ca:EDTA]^{2-}$.

Our analyses resolve the assignments that were unclear in the literature. Lanigan et al.[17] suggested that the $1315–1340\,cm^{-1}$ peaks in the experimental spectra are COO_s^- modes. We suggest that the experimental spectral region $1315–1340\,cm^{-1}$ corresponds to CH_w vibrations and the $1000–1290\,cm^{-1}$ region is a CH_t motion (Figure 6 left). Our analysis clarifies that the dominant mode mixing into metal-bound COO_s^- is the CH_s rather than CH_w.[19] The CH_w mixing with the COO_s^- diminishes from the apo-EDTA to an insignificant level in the metal-bound state. According to our assignments in apo-EDTA, the asymmetrical broad tail in the $1450–1530\,cm^{-1}$ region of the infrared spectrum arises from a distribution of the CH_s

modes, broadened by disorder in the solvent.

We have completed assigning the peaks in the linear spectrum for the three molecules. We found that the CH_s and the COO_s^- modes mix in $[Ca:EDTA]^{2-}$, $[Mg:EDTA]^{2-}$, and apo-EDTA; the CH_w modes mix to a lesser extent. This section also compared the delocalization of COO_a^- versus the localized COO_s^- modes and determined the cause of the asymmetric lineshape in apo-EDTA, $[Ca:EDTA]^{2-}$, and $[Mg:EDTA]^{2-}$ spectra. We also discussed how the C_2 symmetry governs the sagittal and equatorial peak pair positions in the linear spectra of the complexes and that the binding geometry deformation is responsible for the IR peak shapes in the three molecules. Finally, we elucidated some of the unresolved assignments. In the next section, we aim to rationalize the unique coupling features between the different peaks in the 2D-IR spectra of the three molecules and link them to the binding geometry.

3.3 Mixed modes couple, creating cross-peaks

In this section, we will focus on the observed patterns of cross-peaks in the 2D-IR spectra and interpret them with the calculated participation coefficients. Finally, we aim to link the shape of the spectra to the binding geometry of the metal ions.

The 2D-IR spectrum of apo-EDTA reflects a disordered state, whereas those of the complexed molecules show an ordered structure. Disorder in the apo-EDTA structure (C_1 symmetry) leads to the broad diagonal bands and off-diagonal features A, B, and C in the 2D-IR spectrum (Figure 3a), which reflect its conformational flexibility. In the complexes (Figure 3b,c), however, the diagonal bands and the cross-peaks sharpen, indicating the ordering of the acetate groups around the ion.

Couplings between the normal modes cause cross-peaks in the 2D-IR spectra. Our participation analysis shows that the CHH atoms attached to any particular carboxylate participate in more than one normal mode. For example, in the CHH plot of $[Ca:EDTA]^{2-}$ (Figure 5b bottom), normal modes 18 and 21 both contain CH_s motions of the fourth acetate group (row 4). Any excitation of mode 18 involves the CHH atoms, which then causes a

frequency shift in normal mode 21 due to the local mode (CHH) anharmonicity. In the 2D-IR spectrum of $[Ca:EDTA]^{2-}$ (Figure 3b), we therefore expect cross-peaks between mode 18 ($\omega_1 = 1413$) and 21 ($\omega_1 = 1442$) by virtue of the CHH atoms coupling these two normal modes, which we observe (cross-peaks A, B, C). Similarly, we can rationalize the cross-peaks in the apo-EDTA and $[Mg:EDTA]^{2-}$ 2D-IR spectra by examining the CH_s participation coefficients for each of the sagittal (rows 1 and 2) and equatorial (rows 3 and 4) carboxylates. As another example, the 2D-IR spectrum of $[Mg:EDTA]^{2-}$ (Figure 3c) exhibits the expected cross-peak A from the coupling between the normal modes 17 ($\omega_1 = 1408$) and 20 ($\omega_1 = 1435$), which have participation from the same equatorial CHH atoms (Figure 5c bottom, row 3).

Table 2: 2D-IR diagonal peak assignments for the three molecules. Normal modes listed fall within each peakshape. The peak strengths represent the oscillator strength and the cancellation from neighboring diagonal and cross-peaks in the spectrum.

$\omega_1 = \omega_3$ (cm^{-1})	Anharmonicity (cm^{-1})	Major mode	Mixed modes	Normal modes	Peak strength
		$[apo\text{-}EDTA]^{4-}$			
1407	19	COO_s^-	CH_s, CH_w	15–19	strong
1429	N/A	CH_s	–	20–21	weak
1443	N/A	CH_s	–	22–23	faint
		$[Ca:EDTA]^{2-}$			
1413	16	COO_s^-	CH_s	14–19	strong
1435	N/A	CH_s	–	20–21	faint
1442	N/A	CH_s	–	22–23	strong
		$[Mg:EDTA]^{2-}$			
1408	19	COO_s^-	CH_s, CH_w	14–16	strong
1421	23	COO_s^-	CH_s	17–19	medium
1435	N/A	CH_s	–	20–21	weak
1452	N/A	CH_s	–	22–23	strong

No cross-peaks appear between the strong COO_s^- diagonal bands of the sagittal and equatorial carboxylates of $[Mg:EDTA]^{2-}$ (Table 2). These vibrations involve the motion of different atoms, so mechanical coupling is negligible. Through-space coupling of the COO_s^- modes is likely to be small as well. EDTA's COO_a^- modes have negligible through-space

coupling,[19] and the transition dipole moment of COO_s^- is half that of the COO_a^-. In addition, the transition dipoles of the sagittal and equatorial carboxylates are nearly orthogonal (Figure 1). Modes 17 and 18 contain in-phase and out-of-phase combinations of the equatorial COO_s^- vibrations, but the calculated frequency difference is $\sim 1\,cm^{-1}$. This splitting is less than the linewidth, and cross-peaks are also not observed.

There are cross-peaks between the $\omega_1 = 1435\,cm^{-1}$ (modes 20 and 21) and the $\omega_1 = 1452\,cm^{-1}$ (modes 22 and 23) diagonal bands (Table 2). Modes 22 and 23 are in- and out-of-phase motions of the three CHH's attached to each nitrogen, respectively. A terminal sagittal CHH participates in the modes 20, 21, and 22, while the other terminal sagittal CH_s participates in the modes 20 and 23 (Figure 5c). So, both modes 20 and 21 are coupled to modes 22 and 23 by their terminal CHH and should exhibit cross-peaks between the two bands in the 2D-IR spectrum. These anticipated cross-peaks in the $[Mg:EDTA]^{2-}$ 2D-IR spectrum are observed at C, D, and E (Figure 3c).

Our 2D-IR cross-peak and participation coefficient analyses suggest that the coupling between the mixed COO_s^- and CH_s modes is mechanical in origin. We projected the normal modes from a covalently bonded CHH group onto the normal modes of EDTA and its complexes (Section 2.4.3). In the harmonic limit, normal modes are uncoupled. Due to local mode anharmonicity, however, motion of shared atoms can cause couplings between the normal modes. Thus the cross-peaks between the mixed COO_s^- band and the CH_s bands show the effect of mechanical coupling between the carboxylates and their covalently bound CHH groups. In Section 3.4, we will show that charge transfer, which can contribute to cross-peak formation in a 2D-IR spectrum,[53] does not play a critical role in the binding geometry.

The main takeaway from this section is that our vibrational coupling analysis of the 2D-IR spectra suggests that observed cross-peaks are due to mechanical coupling between normal modes due to the shared atoms. The terminal CHH strongly couples the carboxylates and CH_s vibrations. Additionally, we have linked the metal binding geometry to the pattern of

peaks and cross-peaks in the 2D-IR spectra. The absence of through-space coupling in the $[Mg:EDTA]^{2-}$ 2D-IR spectra is due to the small transition dipole moment and orthogonal orientation of the sagittal and equatorial carboxylates.

Table 3: Binding pocket ChElPG partial charges from M05-2X.

Atom	Complex	
	$[Mg:EDTA]^{2-}$	$[Ca:EDTA]^{2-}$
Metal	1.529	1.528
N1	0.418	0.426
N2	0.399	0.432
C	0.614	0.517

3.4 Metal–EDTA binding is dominated by electrostatics but differentiated by ion size

Ion size is a significant factor in the binding geometry. The CH bending modes are indirectly sensitive to this size effect, which differentiates the 2D-IR spectra of the three molecules. Our analysis, however, has not yet considered which components of the binding interaction are important for characterizing the effect of the metal binding on the infrared spectral shapes. To understand what types of interactions influence the ion–binding geometry of EDTA, we calculate the different contributions to the ion–EDTA binding energy through EDA.

In order to quantify the relative importance of electrostatic and non-electrostatic interactions in metal–EDTA binding, we performed both ALMO-EDA and SAPT calculations (Table 4). The qualitative agreement between the two methodologies is surprisingly strong, considering the different reference wavefunctions. The geometric distortion contribution (ΔE_{geom}) for Mg^{2+} is larger than for Ca^{2+} because the EDTA deforms slightly more for the magnesium

[0]The solvation energy component for SAPT is zero as those calculations were performed in the gas phase. The SAPT0 terms have been relabeled according to $\Delta E_{\text{elec}} = E^{(10)}_{elst}$, $\Delta E_{\text{Pauli}} = E^{(10)}_{exch}$, $\Delta E_{\text{disp}} = E^{(20)}_{disp} + E^{(20)}_{exch-disp}$, and $\Delta E_{\text{pol}} = E^{(20)}_{ind,resp} + E^{(20)}_{exch-ind,resp} + \delta^{(2)}_{HF}$. $\Delta E^{\text{SAPT0}}_{\text{int}}$ does not include the charge transfer term due to its calculation as the difference between the dimer and monomer basis induction energies, rather than as the difference between the supersystem and constrained fragment energies (as in ALMO-EDA). However, $\Delta E^{\text{SAPT0}}_{\text{int}}$ *has* been modified to include ΔE_{geom}, which is computed at the HF/def2-TZVP/gas level.

Table 4: Comparison of ALMO-EDA and SAPT components. All values have units of $\mathrm{kcal\,mol^{-1}}$**.**

contribution	ALMO-EDA		SAPT0 (monomer basis)	
($\mathrm{kcal\,mol^{-1}}$)	Mg^{2+}	Ca^{2+}	Mg^{2+}	Ca^{2+}
ΔE_{geom}	22.21	9.05	136.33	96.51
ΔE_{solv}	876.94	772.90	0.00	0.00
ΔE_{elec}	−1108.80	−1027.38	−914.31	−862.97
$\Delta E_{\mathrm{Pauli}}$	98.79	134.57	68.43	102.75
ΔE_{disp}	5.67	−4.36	−3.14	−12.13
ΔE_{pol}	−58.56	−29.32	−189.00	−143.14
ΔE_{CT}	−11.23	−27.56	−5.22	−3.47
ΔE_{int}	−174.98	−172.09	−901.67	−818.99

ion, which sits deeper inside the cavity formed by the EDTA cage ($d_{\mathrm{N-Mg}} = 222\,\mathrm{pm}$), while calcium is only partially inside this cavity ($d_{\mathrm{N-Ca}} = 251\,\mathrm{pm}$).

The solvated electrostatic interaction between fragments is broken down into the gas-phase interaction (ΔE_{elec}) and the solute-solvent correction that screens this interaction (ΔE_{solv}). Despite the large solvent screening effect, the total electrostatic interaction is still larger than any other EDA component and is larger than the total interaction energy. The takeaway is that binding of Mg^{2+} and Ca^{2+} to EDTA is completely dominated by electrostatics, not polarization or charge transfer.

The destabilizing Pauli exchange part of the interaction ($\Delta E_{\mathrm{Pauli}}$) is larger for Ca^{2+} than Mg^{2+}, which is potentially due to both the larger effective ionic radius of Ca^{2+} (100 pm) compared to Mg^{2+} (72 pm) and the absolute position of the ion with respect to EDTA.[75] The energy lowering due to polarization of fragment densities in the presence of other fragments (ΔE_{pol}) is about twice as great for $[Mg{:}EDTA]^{2-}$ than $[Ca{:}EDTA]^{2-}$. This may seem counterintuitive at first, since both the neutral and dication forms of calcium are more polarizable than the respective forms of magnesium. However, this is an energy lowering term, not an observable property like the polarizability, so they are not comparable. Both the more negative polarization and less negative total frozen density interaction ($\Delta E^{(s)}_{\mathrm{geom}} + \Delta E^{(s)}_{\mathrm{frz}}$) for $[Mg{:}EDTA]^{2-}$ indicate that the frozen density state for $[Mg{:}EDTA]^{2-}$ is less energetically

favorable than for $[Ca:EDTA]^{2-}$, again due to the decreased ion–binding pocket distance. The energy lowering due to charge transfer (ΔE_{CT}) is one of the smallest contributors to binding, even for ALMO-EDA.

While ALMO-EDA and SAPT broadly agree, there are two categories of differences between the ALMO-EDA and SAPT results: those where the trends between Mg^{2+} and Ca^{2+} are preserved but the absolute magnitudes are quite different, and those where the trends between Mg^{2+} and Ca^{2+} are reversed or there are sign changes.

For the first category, ΔE_{geom} and ΔE_{pol} are much larger in magnitude for SAPT than for ALMO-EDA. This is because the SAPT calculations use ωB97X-D/def2-TZVP/SMD geometries and not the method native ones. SAPT0 does not account for intramonomer correlation, as it starts from a HF/def2-TZVP/gas reference wavefunction, and Hartree–Fock is expected to underestimate bond lengths and have too-small atomic densities due to its lack of (in this case) dynamic correlation.[76] If the geometries used for SAPT calculations were from HF/def2-TZVP/gas and not ωB97X-D/def2-TZVP/SMD, both ΔE_{geom} and ΔE_{pol} for SAPT should be closer to the ALMO-EDA values.

For the second category, there are two notable qualitative differences between the ALMO-EDA and SAPT results: charge transfer increases going from Mg^{2+} to Ca^{2+} with ALMO-EDA but decreases with SAPT, and for dispersion, both ALMO-EDA and SAPT display the same trend of dispersion becoming more attractive going from Mg^{2+} to Ca^{2+}, but dispersion is actually repulsive for $[Mg:EDTA]^{2-}$ with ALMO-EDA. This is most likely due to the definition of dispersion used in ALMO-EDA, which for ωB97X-D is

$$\begin{aligned}\Delta E_{\text{disp}} = &\left(E_{\omega\text{B97X-D}}[\mathbf{P}_{\text{init}}] - \sum_{A}^{\text{frags}} E_{\omega\text{B97X-D}}[\tilde{\mathbf{P}}_A] \right) \\ &- \left(E_{\text{HF}}[\mathbf{P}_{\text{init}}] - \sum_{A}^{\text{frags}} E_{\text{HF}}[\tilde{\mathbf{P}}_A] \right)\end{aligned} \tag{11}$$

(see equation 2.8 in ref. 70), which includes some amount of correlation from the density functional and not just the empirical dispersion correction, so we expect the SAPT definition

(the same as the opposite-spin MP2 correlation energy[73]) to be more formally justifiable.

Still, due to structural differences in the binding of Mg^{2+} and Ca^{2+} to EDTA, questions remain about how much of each energy interaction term is due to the electron density and size of the ion versus the different EDTA geometries. The origins of the non-electrostatic interaction terms are also unclear. To analyze this, we performed "swapped metal" ALMO-EDA and SAPT calculations (Table 5), where the Mg^{2+} in the $[Mg{:}EDTA]^{2-}$ geometry is replaced with Ca^{2+}, and the Ca^{2+} in the $[Ca{:}EDTA]^{2-}$ geometry is replaced with Mg^{2+}. We find that although electrostatics dominate the binding interaction and the identity of the bound ion determines the EDTA geometry, there is a nuanced dependence of the remaining decomposition terms on the ion identity and EDTA geometry (Table 6).

The partial charges (Table 3) show that ion identity is primarily a size effect and not a nuclear charge effect, since the ChElPG charges for both Mg^{2+} and Ca^{2+} in their optimal binding geometries are effectively identical. We rationalize the dependence of charge transfer being only on ion identity on Mg^{2+} having fewer orbitals that can accept electron density than Ca^{2+}. It is also encouraging that ALMO-EDA and SAPT0 are in agreement between all four ion–EDTA geometry permutations, except for the small $\Delta E_{\mathrm{CT}}^{\mathrm{SAPT0}}$ of $[Ca{:}EDTA]^{2-}$, which is likely an artifact of the definition of charge transfer within the SAPT formalism (Supporting Information), and ΔE_{disp} becoming more favorable for Mg^{2+}-in-$[Ca{:}EDTA]^{2-}$ with ALMO-EDA. Placing Ca^{2+} in the $[Mg{:}EDTA]^{2-}$ cavity gives the expected result of increases in ΔE_{elec}, $\Delta E_{\mathrm{Pauli}}$, and ΔE_{CT}, with Pauli repulsion more than offsetting the favorable increase in the electrostatic and charge transfer interactions. Despite this, Ca^{2+}-in-$[Mg{:}EDTA]^{2-}$ is still a bound complex, indicating that some combination of the components which vary most strongly with changing ion identity ($\Delta E_{\mathrm{Pauli}}$, ΔE_{disp}, and ΔE_{CT}) modulates the metal binding depth and, therefore, controls the EDTA geometry.

Table 5: "Swapped metal" ALMO-EDA and SAPT results. Those columns marked with a star (*) indicate the given metal is used in the complexed geometry belonging to the other metal; for example, "Ca^{2+}*" refers to the Mg^{2+}-bound complexed geometry, but with Mg^{2+} replaced by Ca^{2+}. Otherwise, this is the same as Table 4.

contribution	ALMO-EDA				SAPT0 (monomer basis)			
(kcal mol^{-1})	Mg^{2+}	Mg^{2+}*	Ca^{2+}	Ca^{2+}*	Mg^{2+}	Mg^{2+}*	Ca^{2+}	Ca^{2+}*
ΔE_{geom}	22.21	9.05	9.05	22.21	136.33	96.51	96.51	136.33
ΔE_{solv}	876.94	845.16	772.90	799.05	0.00	0.00	0.00	0.00
ΔE_{elec}	−1108.80	−1001.87	−1027.38	−1178.36	−914.31	−846.66	−862.97	−963.27
ΔE_{Pauli}	98.79	38.00	134.57	342.56	68.43	23.91	102.75	278.74
ΔE_{disp}	5.67	1.35	−4.36	−5.44	−3.14	−1.69	−12.13	−20.55
ΔE_{pol}	−58.56	−29.80	−29.32	−58.41	−189.00	−149.19	−143.14	−194.92
ΔE_{CT}	−11.23	−11.58	−27.56	−47.20	−5.22	−6.41	−3.47	−13.41
ΔE_{int}	−174.98	−149.68	−172.09	−125.60	−901.67	−877.11	−818.99	−763.67

Table 6: Dependence of each energy decomposition term on ion identity, EDTA geometry, or both.

term	dependence
ΔE_{elec}	mostly EDTA geometry
ΔE_{Pauli}	both ion identity and EDTA geometry
ΔE_{disp}	only ion identity
ΔE_{pol}	only EDTA geometry
ΔE_{CT}	only ion identity (ALMO-EDA; SAPT slightly less so)

4 Conclusion

We have assigned the unresolved infrared peaks in the symmetric stretch of EDTA. Using electronic structure theory, we present a method to estimate the mode-mixing in the symmetric stretch region. Participation coefficients resolve the assignments for peak structures seen in the 1000–1650 cm^{-1} region for apo-EDTA, $[\text{Ca:EDTA}]^{2-}$, and $[\text{Mg:EDTA}]^{2-}$. Further analysis with participation coefficients also helps us identify the delocalization in the different CH_t, CH_w, CH_s, and COO^- modes. Energy decomposition analysis shows that electrostatics drive ion binding to EDTA, but binding geometry differences are a consequence of ion size. Five main conclusions are:

(1) We provide a method to untangle the contributions of the CH and COO modes in carboxylate molecules.

(2) From the participation analyses, we assigned the individual infrared peaks as CH_t (1000–1380 cm^{-1}), CH_w (1380–1430 cm^{-1}), CH_s (1420–1650 cm^{-1}), and COO_s (1400–1450 cm^{-1}) modes.

(3) CH mode participation in the symmetric carboxylate stretch region of EDTA makes it a region highly sensitive to cation–induced geometry changes. The ion–induced geometry distortions are reflected in the pattern of CH_s, CH_w, and CH_t participation coefficients.

(4) The observed vibrational bands in both linear and 2D-IR spectra illustrate the sensitivity of the COO_s region to structural differences between Mg^{2+} and Ca^{2+} binding. The distinct splitting of the sagittal and equatorial COO_s bands seen in linear and 2D-IR spectra

correlate directly to tighter binding of Mg^{2+} compared to Ca^{2+}.

(5) EDTA strongly binds both Mg^{2+} and Ca^{2+}, primarily due to electrostatics, even in the presence of solvent screening. Size effects determine the shape of the distorted EDTA, where the depth of the ion in the EDTA pocket is likely modulated by the smaller, non-electrostatic interactions.

Changes in the linear and 2D-IR spectra are connected to the changes in metal-binding geometry. The participation coefficient method provides a new approach to elucidate the detailed information contained in the COO^-_s spectral region. We have linked the changes in metal–binding geometry to the specific patterns in the linear and 2D-IR spectra. Participation coefficient analysis, when applied to the embedded carboxylate interactions in protein active sites, might uncover a more detailed interplay between the ion and the protein[77,78] than is possible with the traditional use of amide and COO^-_a internal probes. Thus, 2D-IR spectroscopy in conjunction with participation analysis may be used to understand the selectivity and specificity of EF-Hand proteins towards Ca^{2+} or Mg^{2+} cations.[3,18,79,80] .

5 Associated content

5.1 Supporting Information

A comparison of monomer- and dimer-basis SAPT results, percent participation coefficient results from the ωB97X-D theory, calculated raw and scaled harmonic frequencies, overlays of experimental and calculated FTIR spectra, calculated geometric parameters, symmetric stretch region assignments, and calculation output files.

6 Author Information

6.1 Corresponding Author

Sean Garrett-Roe *Associate Professor, Department of Chemistry, University of Pittsburgh* Phone (412) 624-1283; `http://orcid.org/0000-0001-6199-8773`; Email sgrpitt.edu

6.2 Notes

The authors declare no competing financial interest.

Acknowledgement

The authors thank the National Science Foundation (CHE-1454105 and CHE-195484). This research was supported in part by the University of Pittsburgh Center for Research Computing through the resources provided. S.M. thanks Dr. Zhe Ren, Dr. Thomas Brinzer, and Mr. Kai Gronborg for their assistance and many useful discussions. E.J.B. thanks cclib [81,82] for the analysis framework.

References

(1) Yumoto, F.; Nara, M.; Kagi, H.; Iwasaki, W.; Ojima, T.; Nishita, K.; Nagata, K.; Tanokura, M. Coordination Structures of Ca2+ and Mg2+ in Akazara Scallop Troponin C in Solution: FTIR Spectroscopy of Side-chain COO- Groups. *Eur. J. Biochem.* **2001**, *268*, 6284–6290.

(2) Nara, M.; Morii, H.; Tanokura, M. Coordination to Divalent Cations by Calcium-binding Proteins Studied by FTIR Spectroscopy. *Biochim. Biophys. Acta - Biomembr.* **2013**, *1828*, 2319–2327.

(3) Suzuki, N.; Imai, L. F.; Kato, Y.; Nagata, K.; Ohashi, Y.; Kuchitsu, K.; Tanokura, M.; Sakamoto, A.; Nara, M.; Nakano, M. et al. Coordination Structures of Mg 2+ and Ca 2+ in Three Types of Tobacco Calmodulins in Solution: Fourier-Transform Infrared Spectroscopic Studies of Side-Chain COO - Groups. *Biopolymers* **2013**, *99*, 472–483.

(4) Grabarek, Z. Insights into Modulation of Calcium Signaling by Magnesium in Calmodulin,

Troponin C and Related EF-Hand Proteins. *Biochim. Biophys. Acta - Mol. Cell Res.* **2011**, *1813*, 913–921.

(5) Alberts, B. *Molecular Biology of the Cell*; CRC Press, 2017.

(6) Christov, C. *Metal-Containing Enzymes*; Advances in Protein Chemistry and Structural Biology; Elsevier Science, 2014.

(7) Dudev, T.; Lim, C. Metal Binding Affinity and Selectivity in Metalloproteins: Insights from Computational Studies. *Annu. Rev. Biophys.* **2008**, *37*, 97–116.

(8) Dudev, T.; Lim, C. Competition among Metal Ions for Protein Binding Sites: Determinants of Metal Ion Selectivity in Proteins. *Chem. Rev.* **2014**, *114*, 538–556.

(9) Dudev, T.; Grauffel, C.; Lim, C. How Pb 2+ Binds and Modulates Properties of Ca 2+ -Signaling Proteins. *Inorg. Chem.* **2018**, *57*, 14798–14809.

(10) Dudev, T.; Ilieva, S.; Doudeva, L. How an electric field can modulate the metal ion selectivity of protein binding sites: insights from DFT/PCM calculations. *Phys. Chem. Chem. Phys.* **2018**, *20*, 24633–24640.

(11) Sawyer, D. T.; Paulsen, P. J. Properties and Infrared Spectra of Ethylenediaminetetraacetic Acid Complexes. I. Alkaline Earth Chelates. *J. Am. Chem. Soc.* **1958**, *80*, 1597–1600.

(12) Sawyer, T.; Tackett, E. Properties and Infrared Spectra of Ethylenediaminetetraacetic Acid Complexes. IV. Structure of Several Metal Chelates in Solution. *J.Phys.Chem* **1960**, *2*, 2390–2394.

(13) Sawyer, D. T.; Tackett, J. E. Properties and Infrared Spectra of Ethylenediaminetetraacetic Acid Complexes. V. Bonding and Structure of Several Metal Chelates in Solution. *J. Am. Chem. Soc.* **1963**, *85*, 2390–2394.

(14) Nakamoto, K.; Morimoto, Y.; Martell, A. E. Infrared Spectra of Aqueous Solutions. III. Ethylenediaminetetraacetic Acid, N-Hydroxyethylethylenediaminetriacetic Acid and Diethylenetriaminepentaacetic Acid. *J. Am. Chem. Soc.* **1963**, *85*, 309–313.

(15) Esteban, M.; Serrano, R.; Vilchez, F. Synthesis and vibrational study of some polydentate ligands. *Spectrochim. Acta Part A Mol. Spectrosc.* **1987**, *43*, 1039–1043.

(16) Mizuguchi, M.; Nara, M.; Kawano, K.; Nitta, K. FT-IR Study of the Calcium-Binding to Bovine α-Lactalbumin. Relationships between the Type of Coordination and Characteristics of the Bands due to the Asp COO- Groups in the Ca2+-Binding Site. *FEBS Lett.* **1997**, *417*, 153–156.

(17) Lanigan, K. C.; Pidsosny, K. Reflectance FTIR Spectroscopic Analysis of Metal Complexation to EDTA and EDDS. *Vib. Spectrosc.* **2007**, *45*, 2–9.

(18) Edington, S. C.; Gonzalez, A.; Middendorf, T. R.; Halling, D. B.; Aldrich, R. W.; Baiz, C. R. Coordination to Lanthanide Ions Distorts Binding Site Conformation in Calmodulin. *Proc. Natl. Acad. Sci.* **2018**, *115*, E3126–E3134.

(19) Edington, S. C.; Baiz, C. R. Vibrational Relaxation in EDTA Is Ion-Dependent. *J. Phys. Chem. A* **2018**, *122*, 6585–6592.

(20) Edington, S. C.; Halling, D. B.; Bennett, S. M.; Middendorf, T. R.; Aldrich, R. W.; Baiz, C. R. Non-Additive Effects of Binding Site Mutations in Calmodulin. *Biochemistry* **2019**, *58*, 2730–2739.

(21) Minnes, L.; Shaw, D. J.; Cossins, B. P.; Donaldson, P. M.; Greetham, G. M.; Towrie, M.; Parker, A. W.; Baker, M. J.; Henry, A. J.; Taylor, R. J. et al. Quantifying Secondary Structure Changes in Calmodulin Using 2D-IR Spectroscopy. *Anal. Chem.* **2017**, *89*, 10898–10906.

(22) Lim, M.; Hamm, P.; Hochstrasser, R. M. Protein Fluctuations are Sensed by Stimulated Infrared Echoes of the Vibrations of Carbon Monoxide and Azide Probes. *Proc. Natl. Acad. Sci. USA* **1998**, *95*, 15315–15320.

(23) Drenth, J. *Principles of Protein X-ray Crystallography*; Springer Advanced Texts in Chemistry; Springer New York, 2002.

(24) Möbius, K.; Savitsky, A. *High-field EPR Spectroscopy on Proteins and Their Model Systems: Characterization of Transient Paramagnetic States*; Royal Society of Chemistry, 2009, 2009; p 375.

(25) Cavanagh, J.; Fairbrother, W. J.; Palmer, A. G.; Skelton, N. J.; Rance, M. *Protein NMR Spectroscopy: Principles and Practice*; Elsevier Science, 2007; p 912.

(26) Markwick, P. R. L.; Malliavin, T.; Nilges, M. Structural Biology by NMR: Structure, Dynamics, and Interactions. *PLoS Comput. Biol.* **2008**, *4*, e1000168.

(27) Shi, Y. A Glimpse of Structural Biology through X-Ray Crystallography. *Cell* **2014**, *159*, 995–1014.

(28) Henzler-Wildman, K.; Kern, D. Dynamic personalities of proteins. *Nature* **2007**, *450*, 964–972.

(29) Kim, Y. S.; Hochstrasser, R. M. Applications of 2D IR Spectroscopy to Peptides, Proteins, and Hydrogen-Bond Dynamics. *J. Phys. Chem. B* **2009**, *113*, 8231–8251.

(30) Ghosh, A.; Tucker, M. J.; Gai, F. 2D IR Spectroscopy of Histidine: Probing Side-chain Structure and Dynamics via Backbone Amide Vibrations. *J. Phys. Chem. B* **2014**, *118*, 7799–805.

(31) Ghosh, A.; Tucker, M. J.; Hochstrasser, R. M. Identification of Arginine Residues in Peptides by 2D-IR Echo Spectroscopy. *J. Phys. Chem. A* **2011**, *115*, 9731–9738.

(32) Reppert, M.; Tokmakoff, A. Computational Amide I 2D IR Spectroscopy as a Probe of Protein Structure and Dynamics. *Annu. Rev. Phys. Chem* **2016**, *67*, 359–86.

(33) Kratochvil, H. T.; Maj, M.; Matulef, K.; Annen, A. W.; Ostmeyer, J.; Perozo, E.; Roux, B.; Valiyaveetil, F. I.; Zanni, M. T. Probing the Effects of Gating on the Ion Occupancy of the K+ Channel Selectivity Filter Using Two-Dimensional Infrared Spectroscopy. *J. Am. Chem. Soc.* **2017**, *139*, 8837–8845.

(34) Baiz, C. R.; Błasiak, B.; Bredenbeck, J.; Cho, M.; Choi, J. H.; Corcelli, S. A.; Dijkstra, A. G.; Feng, C. J.; Garrett-Roe, S.; Ge, N. H. et al. Vibrational Spectroscopic Map, Vibrational Spectroscopy, and Intermolecular Interaction. *Chem. Rev.* **2020**, *120*, 7152–7218.

(35) Deacon, G. B.; Phillips, R. J. Relationships between the Carbon-Oxygen Stretching Frequencies of Carboxylate Complexes and the Typs of Carboxylate Coordination. *Coord. Chem. Rev.* **1980**, *33*, 227–250.

(36) Mizuguchi, M.; Nara, M.; Ke, Y.; Kawano, K.; Hiraoki, T.; Nitta, K. Fourier-Transform Infrared Spectroscopic Studies on the Coordination of the Side-chain COO--groups to Ca2+ in Equine Lysozyme. *Eur. J. Biochem.* **1997**, *250*, 72–76.

(37) Mizuguchi, M.; Fujisawa, R.; Nara, M.; Nitta, K.; Kawano, K. Fourier-Transform Infrared Spectroscopic Study of Ca2+-binding to Osteocalcin. *Calcif. Tissue Int.* **2001**, *69*, 337–342.

(38) Deacon, G.; Huber, F.; Phillips, R. Diagnosis of the nature of carboxylate coordination from the direction of shifts of carbon–oxygen stretching frequencies. *Inorganica Chim. Acta* **1985**, *104*, 41–45.

(39) Jackson, M.; Haris, P. I.; Chapman, D.; Hark, P. I. Fourier Transform Infrared Spectroscopic Studies of Ca(2+)-Binding Proteins. *Biochemistry* **1991**, *30*, 9681–6.

(40) Nara, M.; Tasumi, M.; Tanokura, M.; Hiraoki, T.; Yazawa, M.; Tsutsumi, A. Infrared studies of interaction between metal ions and Ca 2+ -binding proteins. Marker bands for identifying the types of coordination of the side-chain COO- groups to metal ions in pike parvalbumin (pI = 4.10). *FEBS Lett.* **1994**, *349*, 84–88.

(41) Kaposi, A. D.; Fidy, J.; Manas, E. S.; Vanderkooi, J. M.; Wright, W. W. Horseradish peroxidase monitored by infrared spectroscopy: effect of temperature, substrate and calcium. *Biochim. Biophys. Acta - Protein Struct. Mol. Enzymol.* **1999**, *1435*, 41–50.

(42) Nara, M.; Tanokura, M. Infrared Spectroscopic Study of the Metal-coordination Structures of Calcium-binding Proteins. *Biochem. Biophys. Res. Commun.* **2008**, *369*, 225–239.

(43) Erwin, N.; Patra, S.; Winter, R. Probing Conformational and Functional Substates of Calmodulin by High Pressure FTIR Spectroscopy: Influence of Ca 2+ Binding and the Hypervariable Region of K-Ras4B. *Phys. Chem. Chem. Phys.* **2016**, *18*, 30020–30028.

(44) Ganim, Z.; Tokmakoff, A.; Vaziri, A. Vibrational Excitons in Ionophores: Experimental Probes for Quantum Coherence-assisted Ion Transport and Selectivity in Ion Channels. *New J. Phys.* **2011**, *13*, 113030.

(45) Stevenson, P.; Götz, C.; Baiz, C. R.; Akerboom, J.; Tokmakoff, A.; Vaziri, A. Visualizing KcsA Conformational Changes upon Ion Binding by Infrared Spectroscopy and Atomistic Modeling. *J. Phys. Chem. B* **2015**, *119*, 5824–5831.

(46) Strong, S. E.; Hestand, N. J.; Kananenka, A. A.; Zanni, M. T.; Skinner, J. L. IR Spectroscopy Can Reveal the Mechanism of K+ Transport in Ion Channels. *Biophys. J.* **2020**, *118*, 254–261.

(47) Kuroda, D. G.; Hochstrasser, R. M. Dynamic structures of aqueous oxalate and the effects of counterions seen by 2D IR. *Phys. Chem. Chem. Phys.* **2012**, *14*, 6219.

(48) Kuroda, D. G.; Vorobyev, D. Y.; Hochstrasser, R. M. Ultrafast relaxation and 2D IR of the aqueous trifluorocarboxylate ion. *J. Chem. Phys.* **2010**, *132*, 044501.

(49) Kuroda, D. G.; Hochstrasser, R. M. Two-dimensional Infrared Spectral Signature and Hydration of the Oxalate Dianion. *J. Chem. Phys.* **2011**, *135*, 1–12.

(50) Stefan, I. C.; Mandler, D.; Scherson, D. A. In Situ FTIR-ATR Studies of Functionalized Self-Assembled Bilayer Interactions with Metal Ions in Aqueous Solutions. *Langmuir* **2002**, *18*, 6976–6980.

(51) Donaldson, P. M.; Hamm, P. Gold Nanoparticle Capping Layers: Structure, Dynamics, and Surface Enhancement Measured Using 2D-IR Spectroscopy. *Angew. Chemie Int. Ed.* **2013**, *52*, 634–638.

(52) Flaschka, H. A. *EDTA Titrations: An Introduction to Theory and Practice*; Elsevier Science, 2013.

(53) Hamm, P.; Zanni, M. T. *Concepts and Methods of 2D Infrared Spectroscopy*; Cambridge University Press: New York, NY, 2011.

(54) Hamm, P.; Kaindl, R. A.; Stenger, J. Noise Suppression in Femtosecond Mid-Infrared Light Sources. *Opt. Lett.* **2000**, *25*, 1798–1800.

(55) Helbing, J.; Hamm, P. Compact Implementation of Fourier Transform Two-Dimensional IR Spectroscopy Without Phase Ambiguity. *J. Opt. Soc. Am. B* **2011**, *28*, 171.

(56) Zhao, Y.; Truhlar, D. G. Applications and Validations of the Minnesota Density Functionals. *Chem. Phys. Lett.* **2011**, *502*, 1–13.

(57) Chai, J.-D.; Head-Gordon, M. Long-range corrected hybrid density functionals with damped atom–atom dispersion corrections. *Phys. Chem. Chem. Phys.* **2008**, *10*, 6615–6620.

(58) Chai, J.-D.; Head-Gordon, M. Systematic optimization of long-range corrected hybrid density functionals. *J. Chem. Phys.* **2008**, *128*, 84106.

(59) Shao, Y.; Gan, Z.; Epifanovsky, E.; Gilbert, A. T. B.; Wormit, M.; Kussmann, J.; Lange, A. W.; Behn, A.; Deng, J.; Feng, X. et al. Advances in molecular quantum chemistry contained in the Q-Chem 4 program package. *Mol. Phys.* **2015**, *113*, 184–215.

(60) Dasgupta, S.; Herbert, J. M. Standard grids for high-precision integration of modern density functionals: SG-2 and SG-3. *Journal of Computational Chemistry* **2017**, *38*, 869–882.

(61) Marenich, A. V.; Cramer, C. J.; Truhlar, D. G. Universal Solvation Model Based on Solute Electron Density and on a Continuum Model of the Solvent Defined by the Bulk Dielectric Constant and Atomic Surface Tensions. *J. Phys. Chem. B* **2009**, *113*, 6378–6396.

(62) Hanwell, M. D.; Curtis, D. E.; Lonie, D. C.; Vandermeersch, T.; Zurek, E.; Hutchison, G. R. Avogadro: An Advanced Semantic Chemical Editor, Visualization, and Analysis Platform. *J. Cheminform.* **2012**, *4*, 17.

(63) Sutton, C. C. R.; da Silva, G.; Franks, G. V. Modeling the IR Spectra of Aqueous Metal Carboxylate Complexes: Correlation between Bonding Geometry and Stretching Mode Wavenumber Shifts. *Chem. - A Eur. J.* **2015**, *21*, 6801–6805.

(64) Sutton, C. C. R.; Franks, G. V.; Da Silva, G. Modeling the Antisymmetric and Symmetric Stretching Vibrational Modes of Aqueous Carboxylate Anions. *Spectrochim. Acta - Part A Mol. Biomol. Spectrosc.* **2015**, *134*, 535–542.

(65) Katsyuba, S. A.; Zvereva, E. E.; Burganov, T. I. Is There a Simple Way to Reliable Simulations of Infrared Spectra of Organic Compounds? *J. Phys. Chem. A* **2013**, *117*, 6664–6670.

(66) Katsyuba, S. A.; Spicher, S.; Gerasimova, T. P.; Grimme, S. Fast and Accurate Quantum Chemical Modeling of Infrared Spectra of Condensed-Phase Systems. *J. Phys. Chem. B* **2020**, *124*, 6664–6670.

(67) Farrokhpour, H.; Jouypazadeh, H. Description of adenine and cytosine on Au(111) nano surface using different DFT functionals (PW91PW91, wB97XD, M06-2X, M06-L and CAM-B3LYP) in the framework of ONIOM scheme: Non-periodic calculations. *Chem. Phys.* **2017**, *488-489*, 1–10.

(68) Semidalas, E.; Chrissanthopoulos, A. Computational study of structural, vibrational and electronic properties of the highly symmetric molecules M4S6 (M = P, As, Sb, Bi). *Comput. Theor. Chem.* **2019**, *1149*, 41–48.

(69) Horn, P. R.; Mao, Y.; Head-Gordon, M. Probing non-covalent interactions with a second generation energy decomposition analysis using absolutely localized molecular orbitals. *Phys. Chem. Chem. Phys.* **2016**, *18*, 23067–23079.

(70) Horn, P. R.; Mao, Y.; Head-Gordon, M. Defining the contributions of permanent electrostatics, Pauli repulsion, and dispersion in density functional theory calculations of intermolecular interaction energies. *J. Chem. Phys.* **2016**, *144*, 114107.

(71) Mao, Y.; Loipersberger, M.; Kron, K. J.; Derrick, J. S.; Chang, C. J.; Sharada, S. M.; Head-Gordon, M. Consistent inclusion of continuum solvation in energy decomposition analysis: theory and application to molecular CO2 reduction catalysts. *Chem. Sci.* **2021**, 1398–1414.

(72) Hohenstein, E. G.; Sherrill, C. D. Density fitting and Cholesky decomposition approximations in symmetry-adapted perturbation theory: Implementation and application to probe the nature of π-π interactions in linear acenes. *J. Chem. Phys.* **2010**, *132*, 184111.

(73) Hohenstein, E. G.; Parrish, R. M.; Sherrill, C. D.; Turney, J. M.; Schaefer, H. F. Large-scale symmetry-adapted perturbation theory computations via density fitting

and Laplace transformation techniques: Investigating the fundamental forces of DNA-intercalator interactions. *J. Chem. Phys.* **2011**, *135*, 174107.

(74) Smith, D. G. A.; Burns, L. A.; Simmonett, A. C.; Parrish, R. M.; Schieber, M. C.; Galvelis, R.; Kraus, P.; Kruse, H.; Di Remigio, R.; Alenaizan, A. et al. PSI4 1.4: Open-source software for high-throughput quantum chemistry. *J. Chem. Phys.* **2020**, *152*, 184108.

(75) Shannon, R. D. Revised effective ionic radii and systematic studies of interatomic distances in halides and chalcogenides. *Acta Crystallogr. Sect. A* **1976**, *32*, 751–767.

(76) Helgaker, T.; Gauss, J.; Jørgensen, P.; Olsen, J. The prediction of molecular equilibrium structures by the standard electronic wave functions. *J. Chem. Phys.* **1997**, *106*, 6430–6440.

(77) Nakashige, T. G.; Bowman, S. E. J.; Zygiel, E. M.; Drennan, C. L.; Nolan, E. M. Biophysical Examination of the Calcium-Modulated Nickel-Binding Properties of Human Calprotectin Reveals Conformational Change in the EF-Hand Domains and His 3 Asp Site. *Biochem.* **2018**, *57*, 4155.

(78) Halling, D. B.; Liebeskind, B. J.; Hall, A. W.; Aldrich, R. W. Conserved Properties of Individual Ca2+-Binding Sites in Calmodulin. *Proc. Natl. Acad. Sci. - PNAS* **2016**, *113*, E1216–E1225.

(79) Grabarek, Z. Structural Basis for Diversity of the EF-hand Calcium-binding Proteins. *J. Mol. Biol.* **2006**, *359*, 509–525.

(80) Grabarek, Z. Structure of a Trapped Intermediate of Calmodulin: Calcium Regulation of EF-hand Proteins from a New Perspective. *J. Mol. Biol.* **2005**, *346*, 1351–1366.

(81) O'boyle, N. M.; Tenderholt, A. L.; Langner, K. M. cclib: A library for package-independent computational chemistry algorithms. *J. Comput. Chem.* **2008**, *29*, 839–845.

(82) Berquist, E.; Hutchison, G.; Langner, K. M.; O'Boyle, N. M.; Tenderholt, A. L.; Upadhyay, S. Release of cclib version 1.7. 2021.

TOC Graphic